JULY 1969

L-87-69-1

TECHNICAL SUMMARY REPORT

EFFECTS OF SHOCK-INDUCED SEPARATION

Prepared by

LARS E. ERICSSON
Senior Staff Engineer, Engineering Technology

J. PETER REDING
Research Specialist, Aero-Thermodynamics

ROLF A. GUENTHER
Senior Aerodynamics Engineer, Aero-Thermodynamics

Prepared under Contract NAS 8-20354

N70-15796
(ACCESSION NUMBER) (THRU)
68 1
(PAGES) (CODE)
CR-107673 31
(NASA CR OR TMX OR AD NUMBER) (CATEGORY)
FACILITY FORM 602

Lockheed

MISSILES & SPACE COMPANY
A GROUP DIVISION OF LOCKHEED AIRCRAFT CORPORATION
SUNNYVALE, CALIFORNIA

L-87-69-1

Technical Summary Report

EFFECTS OF SHOCK-INDUCED SEPARATION

By Lars E. Ericsson, J. Peter Reding,
and Rolf A. Guenther

July 1969

Prepared under Contract NAS 8-20354 by
Lockheed Missiles & Space Company
Sunnyvale, California

for

NATIONAL AERONAUTICS AND SPACE ADMINISTRATION

ABSTRACT

The effects of shock-induced boundary-layer separation on launch vehicle aerodynamics have been studied. At high subsonic speeds, local supersonic flow regions existing aft of cone-cylinder shoulders are terminated by a normal shock. The resulting boundary-layer separation is shown to change the vehicle aerodynamics and can drastically affect the launch vehicle dynamics. At supersonic speeds, boundary-layer separation is caused by shocks generated by interstage conical fairings. This flare-shock-induced separation does not have the classically assumed axisymmetry, but contains discrete vortices, requiring a reevaluation of existing analytic methods. It is found that a formulation is possible for the aeroelastic characteristics of Saturn launch vehicles that in most cases will give satisfactory predictions. Further work, however, is needed to align the analytic methods with this new more realistic structure of separated flow.

PRECEDING PAGE BLANK NOT FILMED

SUMMARY

The results of a study to refine analytic methods for determination of the aeroelastic characteristics of Saturn launch vehicles are reported. The quasi-steady lumped-time-lag theory developed earlier is extended to include effects of shock-induced separation where accelerated-flow induced delays of the flow separation, especially in the case of terminal normal shocks in mixed flow regions, can have appreciable effects on the elastic vehicle dynamics. Some of the results of the study have already been reported in detail in interim reports. In that case the results are only summarized in the present report, but otherwise the results of the study are reported on in full.

It is found that the classical picture of axisymmetric separated flow which experiences small perturbations from axisymmetry at angle-of-attack is completely false. As a rule, the shock-induced separated flow regions contain large-scale vortices already at zero angle-of-attack, and the vortex geometry is changed dramatically, and not perturbed only slightly, when the angle-of-attack deviates from zero.

The impact of this new flow picture on previously developed analytic tools is discussed. It is found that the computer program for aeroelastic characteristics of Saturn launch vehicles as it can presently be formulated is sufficient for most applications. However, there are limitations which should be removed. A more complete formulation of the submerged body loads is needed to account for the effects of the discrete vortices contained in the viscous shear layer.

PRECEDING PAGE BLANK NOT FILMED

CONTENTS

Section		Page
	ABSTRACT	iii
	SUMMARY	v
	ILLUSTRATIONS	viii
1	INTRODUCTION	1
2	DISCUSSION OF ANALYSIS AND RESULTS	3
	2.1 Methodology	3
	2.2 Unsteady Terminal Shock Effects	6
	2.3 Flow Visualization Studies	10
	2.4 Static and Dynamic Measurements	26
	2.5 Impact on Elastic Body Calculations	34
3	CONCLUSIONS	39
4	RECOMMENDATION FOR FUTURE STUDY	41
5	REFERENCES	43
Appendix		
A	NOMENCLATURE	47
B	SELF-SUSTAINED SHOCK OSCILLATIONS	51

PRECEDING PAGE BLANK NOT FILMED

ILLUSTRATIONS

Figure		Page
1	Correlation of Length of Separation for Laminar, Transitional and Turbulent Boundary Layers (Ref. 10)	4
2	Correlation of Pressure Distribution for Laminar Separation for Various Model Configurations and Reynolds Numbers; $M_0 = 2.3$ (Ref. 11)	5
3	Effect of Angle-of-Attack and Cone Angle on the Aerodynamic Characteristics at $M_\infty = 0.89$ of a Cone-Cylinder Body With Separated Flow	7
4	Terminal-Shock Location on a 20° Cone-Cylinder Body	
	a. Effect of Angle-of-Attack, $M_\infty = 0.95$	8
	b. Effect of Mach Number, $\alpha = 0$	8
5	Pressure Decay $P(\xi)$ From Shoulder Pressure P_C at $\alpha = 0$	9
6	Terminal-Shock Location in Inviscid and Viscous Flow on Cone-Cylinder Bodies at $\alpha = 0$	11
7	Normal Force Derivatives Induced by the Terminal-Shock Movement on a 20° Cone-Cylinder Body at $\alpha = 0$ and High Subsonic Mach Numbers	12
8	Effect of Complete Leeward-Side Flow Separation on the Damping of an Elastic Vehicle Oscillating in Its Second Bending Mode at Various Nose Amplitudes	13
9	Aerodynamic Damping Measured on an 8-Percent Elastic Model of Saturn I, Block II Vehicle With a Jupiter Nose	14
10	China Clay Flow Patterns, $\xi_C = 2.0$, $M = 1.2$	
	a. $\alpha = 0$	15
	b. $\alpha = 4°$	15
11	China Clay Flow Patterns, $\xi_C = 2.0$, $\alpha = 0$, $M = 1.2$ (Re-run)	17

Figure		Page
12	Flow Patterns for Nose-Induced Separation $\xi_C = 1.0$, M = 0.9	
	a. $\alpha = 0$, $\delta_F = 0$	18
	b. $\alpha = 0$, $\delta_F = -4°$	18
	c. $\alpha = 4°$, $\delta_F = 0$	18
	d. $\alpha = 4°$, $\delta_F = -4°$	18
13	Bottom or Windward Side Flow Patterns, $\xi_C = 1.0$, M = 0.9	
	a. $\alpha = 0$, $\delta_F = -4°$	19
	b. $\alpha = 4°$, $\delta_F = -4°$	19
14	Flow Model for Nose-Induced Separation	20
15	Nose-Induced Separation Winward Vortex Pair, $\alpha = 4°$	
	a. $\xi_C = 1.0$, M = 1.2	21
	b. $\xi_C = 2.0$, M = 0.9	21
16	Effect of Angle-of-Attack on Retarded Separation Flow Patterns, $\xi_C = 4.5$, M = 0.9	
	a. $\alpha = 0°$, $\delta_F = -4°$	23
	b. $\alpha = 4°$, $\delta_F = -4°$	23
17	Shock-Induced Separation Upstream Communication Flow Patterns, M = 0.9, $\alpha = 0°$, $\delta_F = -4°$	
	a. $\xi_C = 2.0$	24
	b. $\xi_C = 4.5$	24
18	Shock-Induced Separation Upstream Communication Flow Model	25
19	Effect of Upstream Communication on Shock-Induced Separation Flow Patterns at $\alpha = 4°$, M = 1.2, $\xi_C = 4.5$	
	a. $\alpha = 4°$, $\delta_F = 0$	27
	b. $\alpha = 4°$, $\delta_F = -4°$	27
20	Effect of Upstream Communication on Shock-Induced Separated Flow Patterns at $\alpha = 4°$, M = 1.2, ξ = 2.0	
	a. $\alpha = 4°$, $\delta_F = 0$	28
	b. $\alpha = 4°$, $\delta_F = -4°$	28
21	Typical Flare Damping Results	
	a. $\xi_C = 3.5$	32
	b. $\xi_C = 1.0$	32

Figure		Page
22	Comparison of Static and Dynamic Results	33
23	Flare Normal Force Derivatives at M = 0.9	35
24	Flare Normal Force Derivatives at M = 1.2	36
25	Effects of Shock-Induced Separation on Thickness of Viscous Layer	37
B-1	Separated Flow Profiles and Pressure Distribution in a Compression Corner	51
B-2	Saturn V Plume-Induced Separations	
	a. H = 150,000 ft; M = 5.05; U = 5500 ft/sec	58
	b. H = 180,000 ft; M = 6.15; U = 6600 ft/sec	58

Section 1
INTRODUCTION

The separated flow regions on the Saturn Apollo launch vehicle generated by the tower-mounted escape rocket and interstage conical fairings can have a dominant influence on the elastic vehicle dynamics (Ref. 1). Because the full-scale vehicle is likely to have undergone design changes after the freeze of the model design, an aeroelastic wind tunnel test can often not be extrapolated to full scale without an analytic theory that includes the combined effects of changed geometry, mode shape, and vehicle trajectory. In view of these difficulties, Marshall Space Flight Center (MSFC) contracted Lockheed Missiles & Space Company to develop the needed analytic means (Contracts NAS 8-5338 and NAS 8-11238).

The quasi-steady-constant-time-lag theory developed by LMSC proved capable of predicting the aeroelastic characteristics measured in the wind tunnel test (Ref. 2). Full-scale characteristics could, therefore, be predicted with confidence by analytic extrapolation from the wind-tunnel data (Ref. 3). Later checks of the individual separated flow regions showed that the adverse effects of the escape rocket wake on escape vehicle dynamics is well predicted by the LMSC theory (Ref. 4).

The present work is aimed to check in detail another type of separated flow existing on the Saturn Apollo launch vehicles, i.e., the shock-induced boundary-layer separation. The shock can either be the normal shock terminating a local supersonic speed region at subsonic vehicle velocities or the oblique shock generated by a conical interstage fairing at supersonic speed. A review was made of existing theoretical treatments of shock-induced separation and their agreement with experimental results (Ref. 5), and the shock-induced separation on cylinder-flare bodies was investigated by controlled experiments (Ref. 6). The steady and unsteady aerodynamic effects caused by the terminal shock on cone-cylinder forebodies at high subsonic speeds were the subject

of another interim report (Ref. 7), and the results were applied to the analysis of the biconic payload shroud characteristics on the Saturn IB launch vehicle performed under Contract NAS 8-11238 (Refs. 4 and 8). As reported in Ref. 9, the modifications of the aeroelastic computer codes needed to accommodate the results of the present effort for a more realistic treatment of shock-induced separation, including upstream communication effects were incorporated together with the various other refinements resulting from the efforts under Contract NAS 8-11238.

The present report summarizes the results detailed in the above interim reports (Refs. 5, 6, and 7). However, since the results of a shock oscillation analysis and of experimental and analytic investigations of nonaxisymmetric flare-induced flow separation have not been reported previously, full details will be provided in this report.

Section 2
DISCUSSION OF ANALYSIS AND RESULTS

2.1 METHODOLOGY

When model test data are used to predict full-scale aerodynamics, the scaling problem always causes concern, especially when flow separation is involved. As established by review of the literature on separated flow (Ref. 5), it is now well accepted that both turbulent and laminar separations increase with increasing Reynolds number. Since the turbulent separation is much smaller in extent than the laminar, the effect of Reynolds number must be the opposite when boundary-layer transition occurs in or near the separated flow region. The data by Needham and Stollery (Ref. 10), as well as the findings of other investigators, indicate that the effect of Reynolds number in the latter case is an order of magnitude stronger than in the case of truly laminar or turbulent boundary layer separations (Fig. 1). The great similarity between the separation length dependence on Reynolds number (Re) and the classical dependence of skin friction (c_f), $c_f = f(Re)$, is not coincidental. Chapman and others (Ref. 11) have shown that the separated flow length scale can be normalized using the local skin friction to take care of Reynolds number effects (Fig. 2).

The prime motivation for the review of theoretical treatments of separated flow (Ref. 5) was to find a basis for an analytic formulation of the unsteady behavior of shock-induced separation. Of particular concern was to determine under what conditions self-sustained shock oscillations would be possible. Appendix B defines this so-called critical frequency; Trilling's incident shock treatment (Ref. 12) is extended to the separation in a compression corner. It was found that the exhaust plume-induced separation on Saturn V at high altitudes could have a critical frequency near the range of the so-called POGO oscillation. Consequently, extensive oscillations of the separation pocket and the associated oblique shock might be possible as a result of coupling

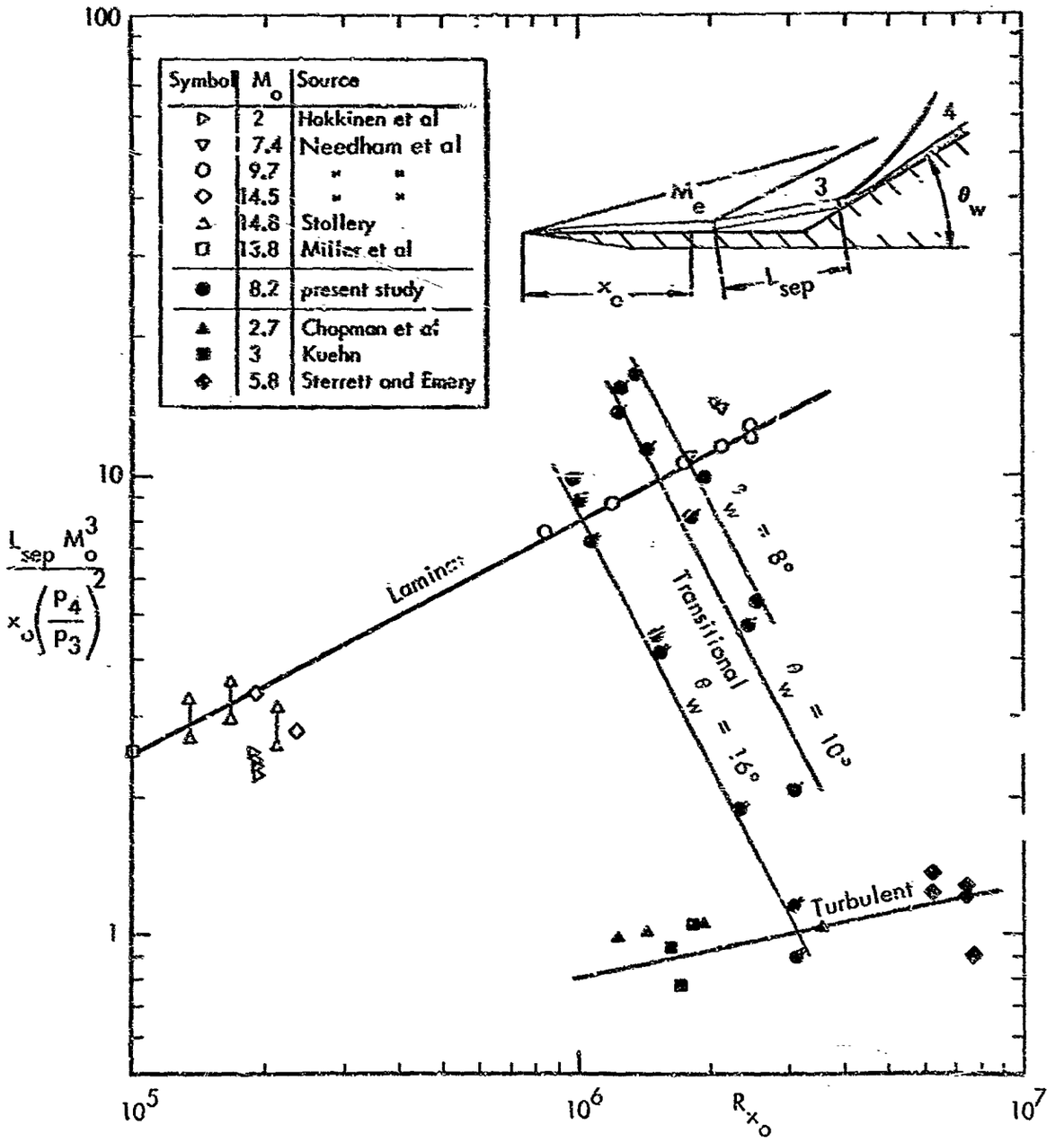


Fig. 1 Correlation of Length of Separation for Laminar, Transitional and Turbulent Boundary Layers (Ref. 10)

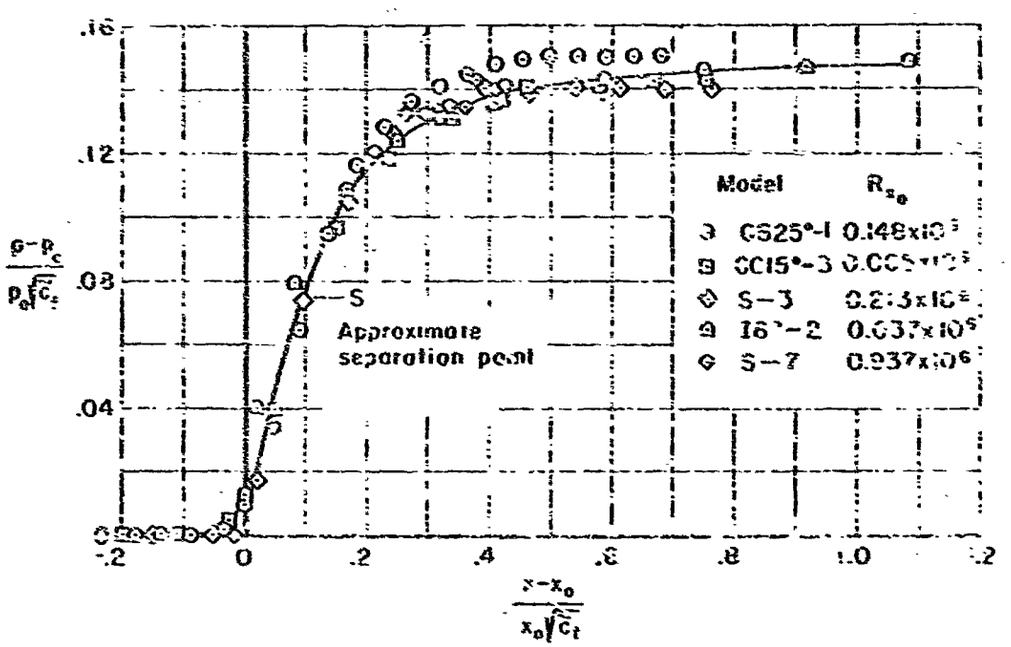


Fig. 2 Correlation of Pressure Distribution for Laminar Separation for Various Model Configurations and Reynolds Numbers; $M_o = 2.3$ (Ref. 11)

between the POGO oscillation and the self-sustained oscillations of the plume induced separated flow "pocket". However, as will be shown later, this "two-dimensional" treatment of a separated flow region is unrealistic.

2.2 UNSTEADY TERMINAL SHOCK EFFECTS

The cone-cylinder is a payload shroud geometry often suggested by both the aerodynamicist and the aeroelastician because of its "clean" aerodynamic characteristics. It is true that slender cone-cylinder bodies normally do not cause any aerodynamic problems. However, there is one exception. At high subsonic Mach numbers, the normal shock terminating the local supersonic speed region aft of the cone-cylinder shoulder causes boundary-layer separation (Ref. 13 and Fig. 3). When the angle-of-attack is increased above a critical value, the leeward side separation jumps forward to the cone-cylinder shoulder. The large discontinuous load change can be appreciated by comparing it with the effect of increasing the angle of attack from $\alpha = 0°$ to $\alpha = 2°$.

The jump to complete leeward side separation occurs at higher angles-of-attack the more slender the forebody is. At angle-of-attack, the leeward side shock moves forward of the windward side shock generating a negative cylinder load (Fig. 4a). This is contrary to the expected effect of the increased leeward side Mach number at angle-of-attack, as an increase in free stream Mach number moves the shock back (Fig. 4b). The forward movement of the leeward side shock and the associated boundary-layer separation result because the leeward side boundary layer is thickened and weakened through forebody crossflow at the same time as the adversity of the pressure gradient is increased due to the increased suction peak on the leeward side cone-cylinder shoulder.

Reference 7 shows how the inviscid shock position can be computed and, thereby, the separation induced effects can be determined. Figure 5 shows how application of the exponential decay concept used by Syvertson and Dennis at supersonic speed (Ref. 14)

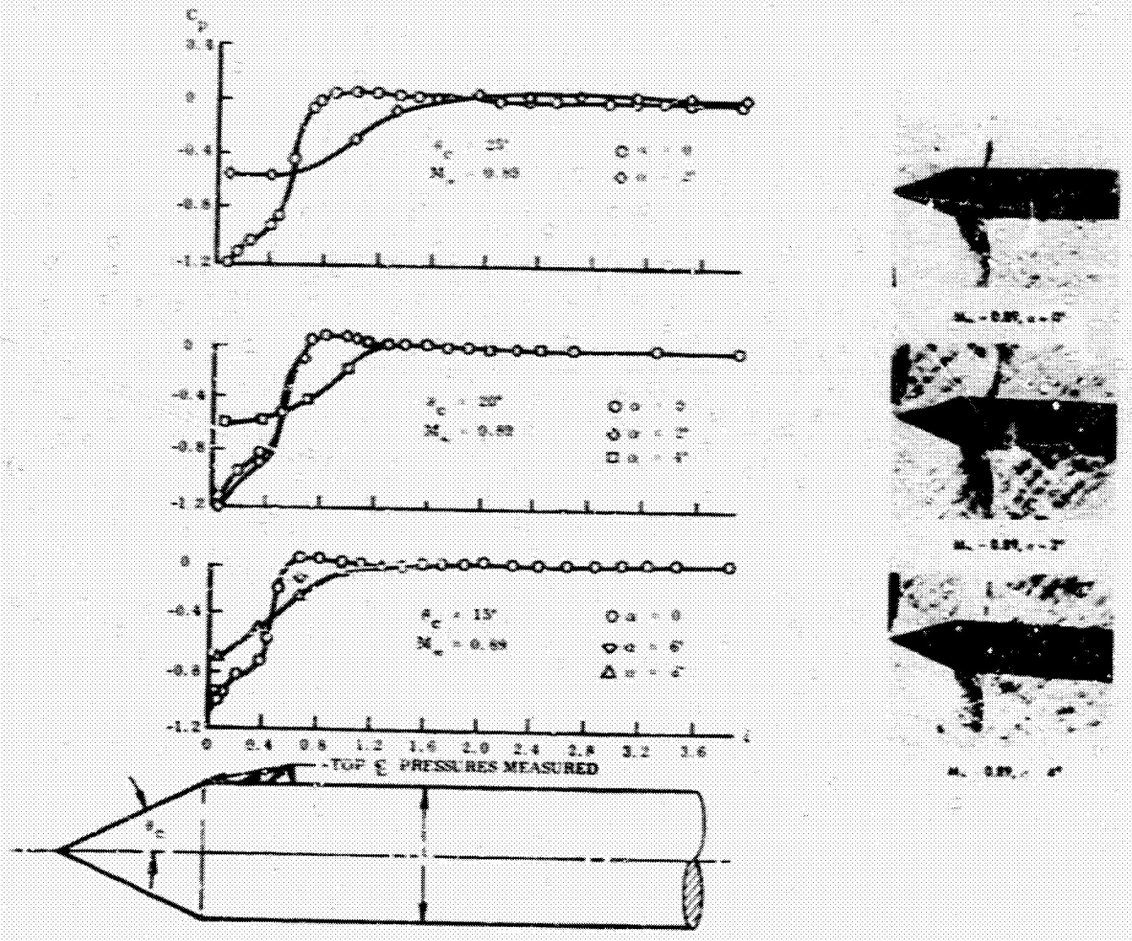


Fig. 3 Effect of Angle-of-Attack and Cone Angle on the Aerodynamic Characteristics at $M_\infty = 0.89$ of a Cone-Cylinder Body With Separated Flow

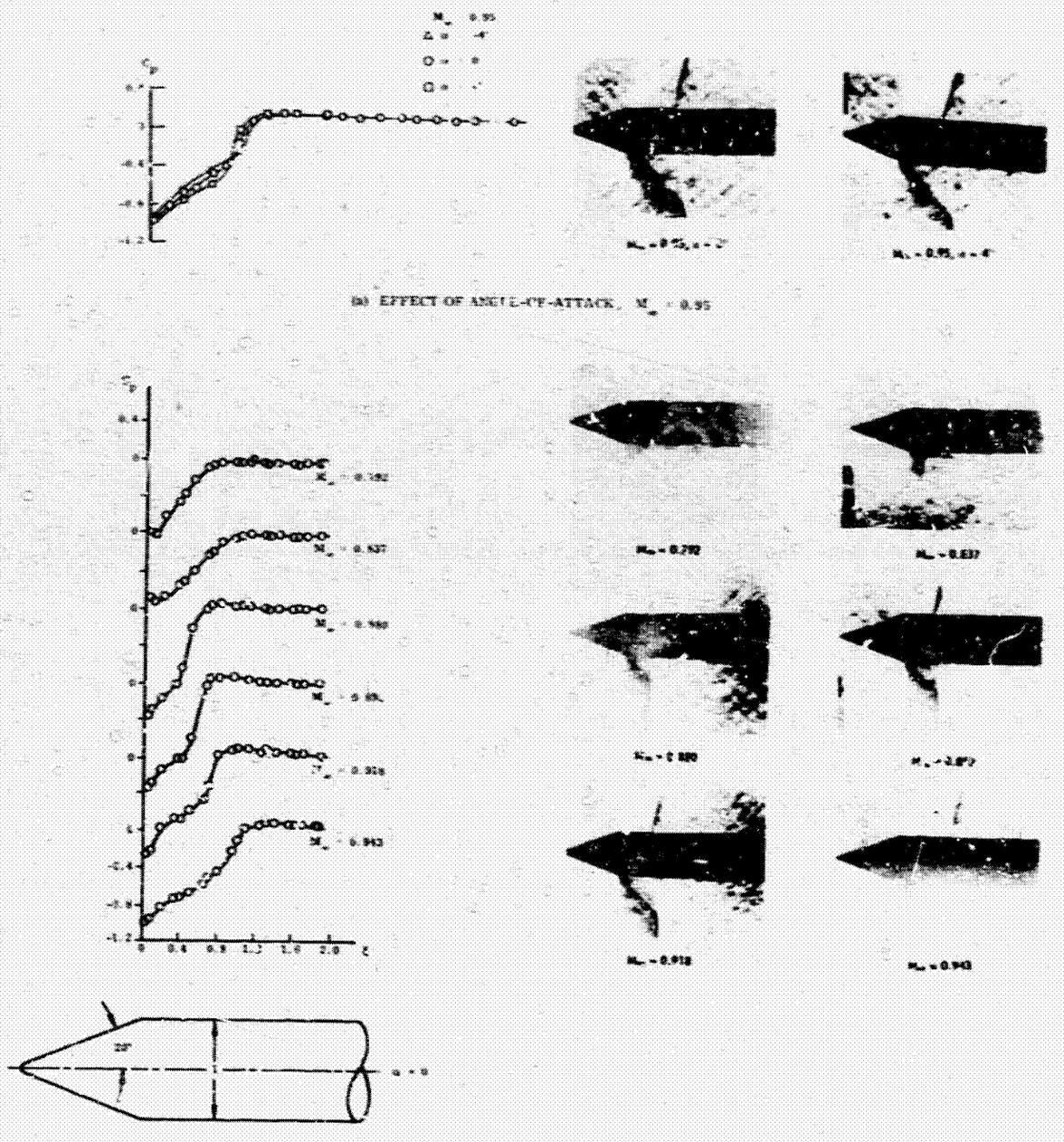
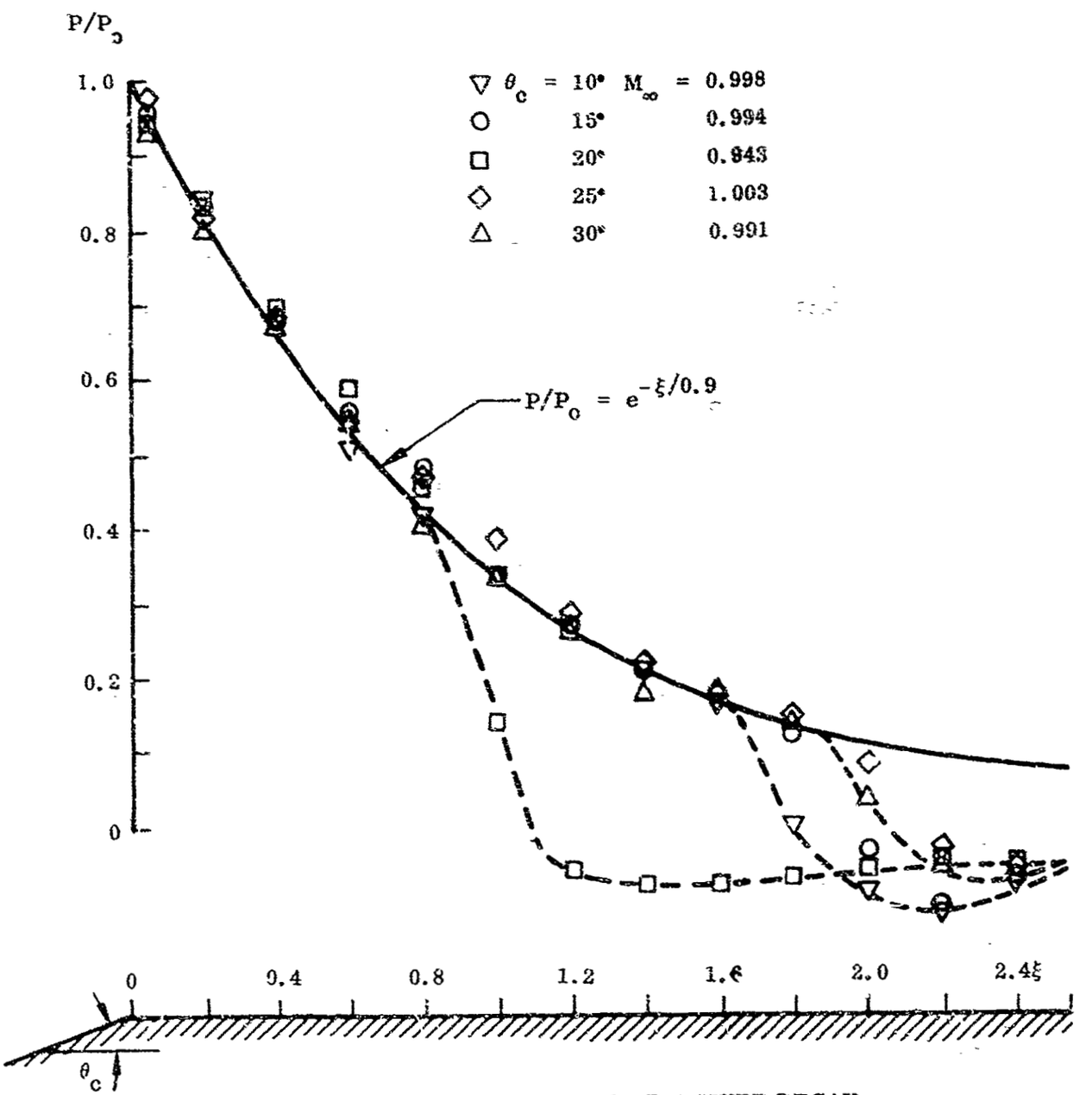


Fig. 4 Terminal-Shock Location on a 20° Cone-Cylinder Body



(a) EFFECT OF CONE ANGLE ON PRESSURE DECAY

Fig 5 Pressure Decay $P(\xi)$ From Shoulder Pressure P_o at $\alpha = 0$

can enable one to describe the normalized pressure distribution aft of the cone-cylinder shoulder by one simple analytic curve.

Assuming free stream pressure behind the normal shock, its axial location is determined, and the separation-induced shock movement can be extracted from the experimental data (Fig. 6). Thus, the separation-induced aerodynamic force derivatives can be computed (Fig. 7).

In the unsteady case, the boundary-layer buildup is delayed through finite convection time lag and the adverse pressure gradient buildup is delayed through accelerated flow effects (Ref. 7). As a result, moderate statically stabilizing separation-induced forces can have large undamping or dynamically destabilizing effects. In the case of the sudden complete leeward side separation, the adverse dynamic effect can become especially critical (Fig. 8). The experimentally observed sudden loss of aerodynamic damping of a Saturn I booster with Jupiter nose shroud was probably caused by this sudden separation phenomenon (Fig. 9).

2.3 FLOW VISUALIZATION STUDIES

In conjunction with the theoretical investigation of shock-induced separation, an experimental test program was undertaken to measure the upstream communication velocity in regions of shock-induced separation and its effect on the flare damping. Before any quantitative data were acquired, a flow visualization study was undertaken to precisely determine separation locations for the placement of instrumentation. The flow visualization results were dramatic. They revealed the existence of large scale vorticity in a plane orthogonal to that assumed in the classical axisymmetric model. (Coe has also observed a similar phenomenon, Ref. 15.) These vortex patterns proved to be extremely sensitive to angle-of-attack. The two pairs of circumferentially distributed vortices observed at $\alpha = 0°$ (M = 1.2, and cylinder length $\xi_C = 2$) became a single leeward side pair at $\alpha = 4°$ (Fig. 10). These strong leeward side vorticies appeared to be fed from the windward reattachment zone and were shed into

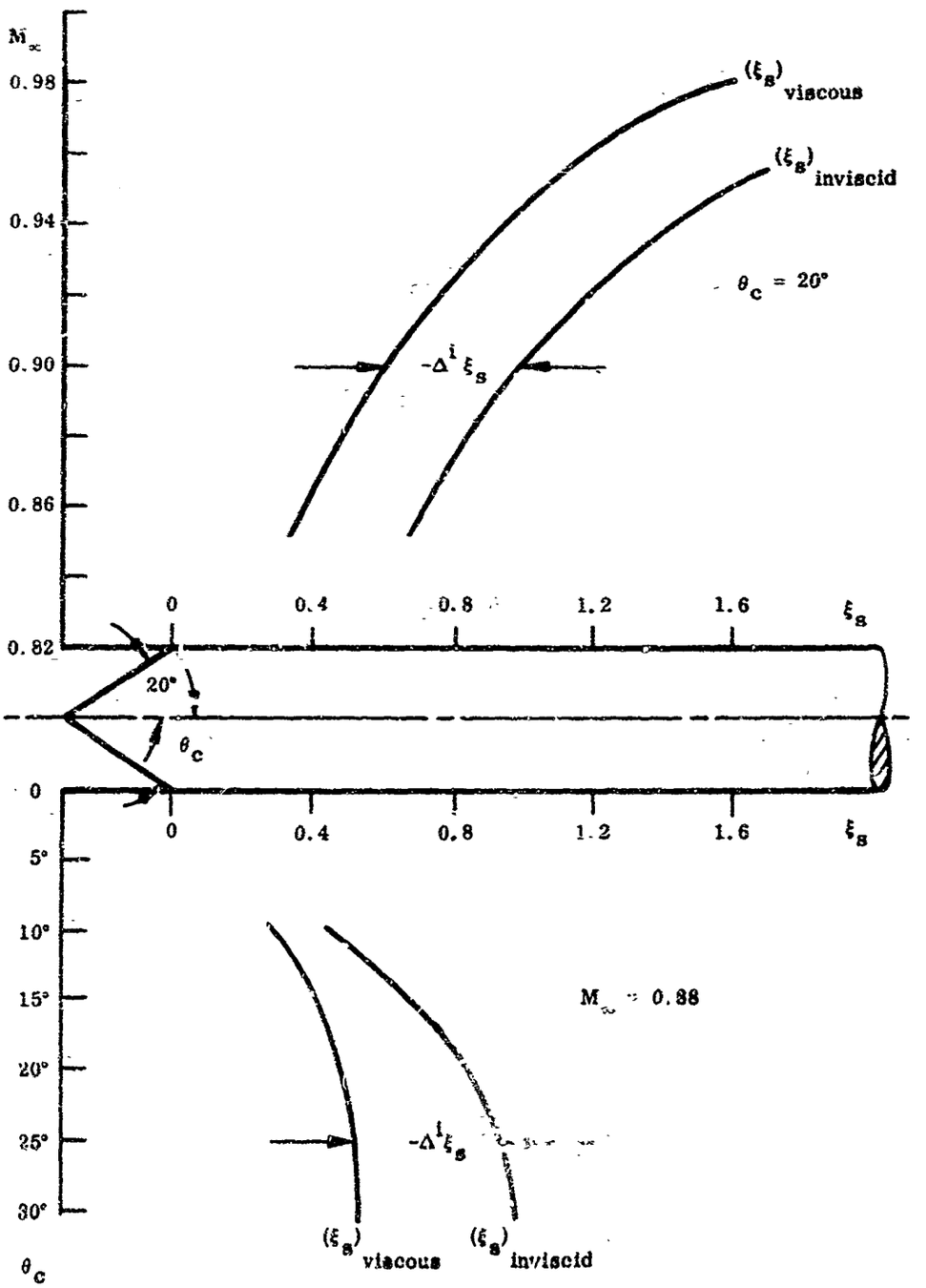


Fig. 6 Terminal-Shock Location in Inviscid and Viscous Flow on Cone-Cylinder Bodies at $\alpha = 0$

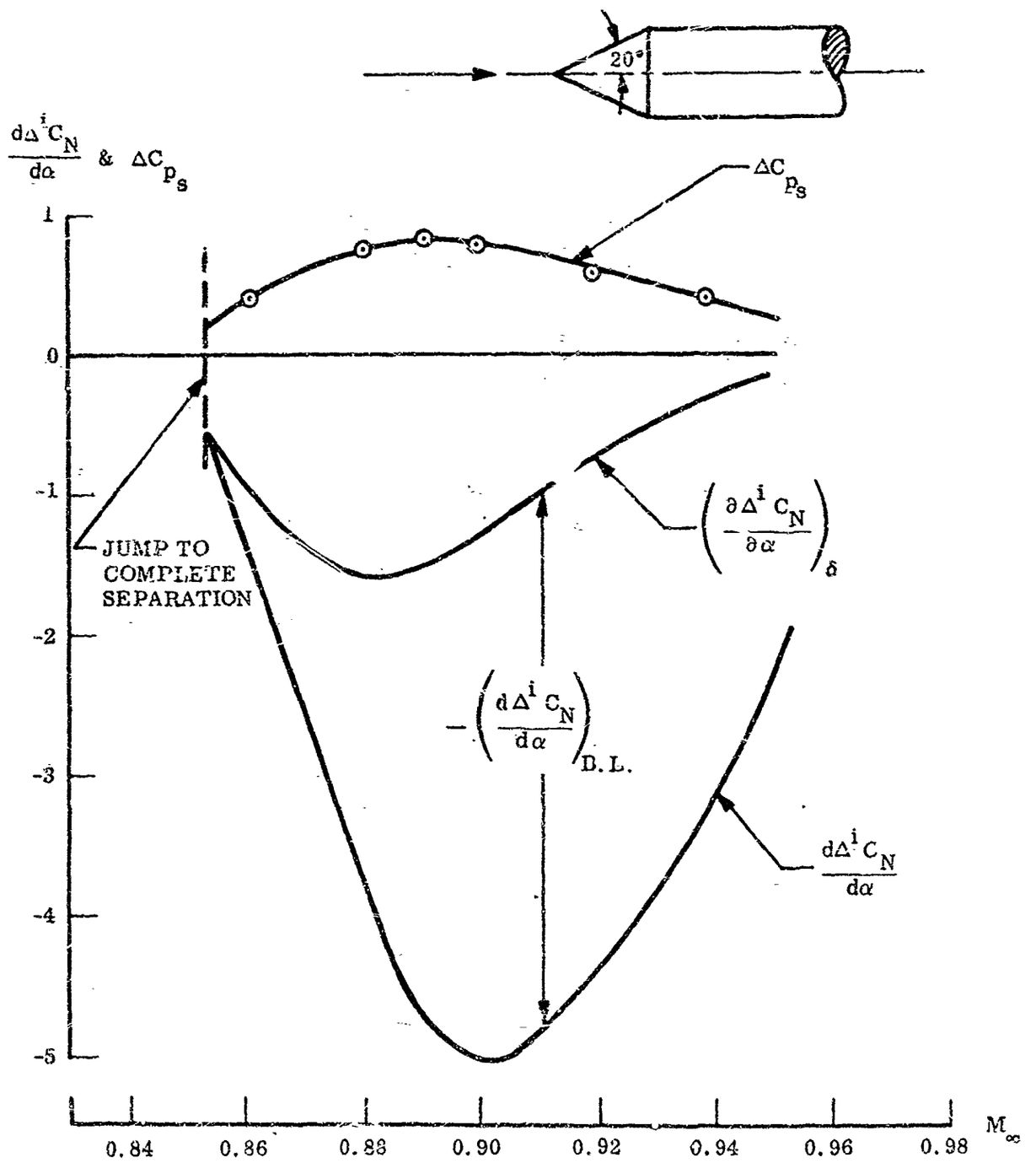


Fig. 7 Normal Force Derivatives Induced by the Terminal-Shock Movement on a 20° Cone-Cylinder Body at $\alpha = 0$ and High Subsonic Mach Numbers

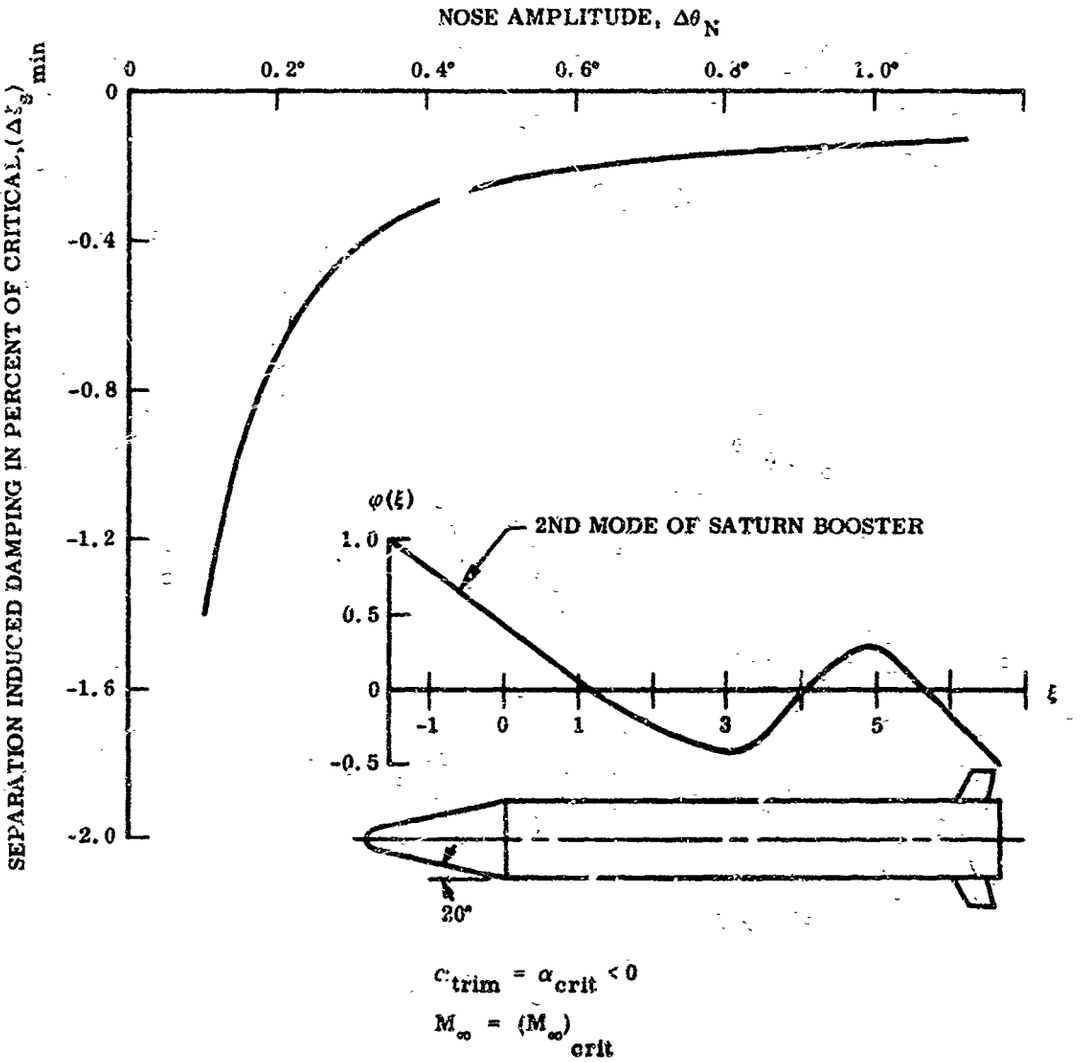


Fig. 8 Effect of Complete Leeward-Side Flow Separation on the Damping of an Elastic Vehicle Oscillating in Its Second Bending Mode at Various Nose Amplitudes

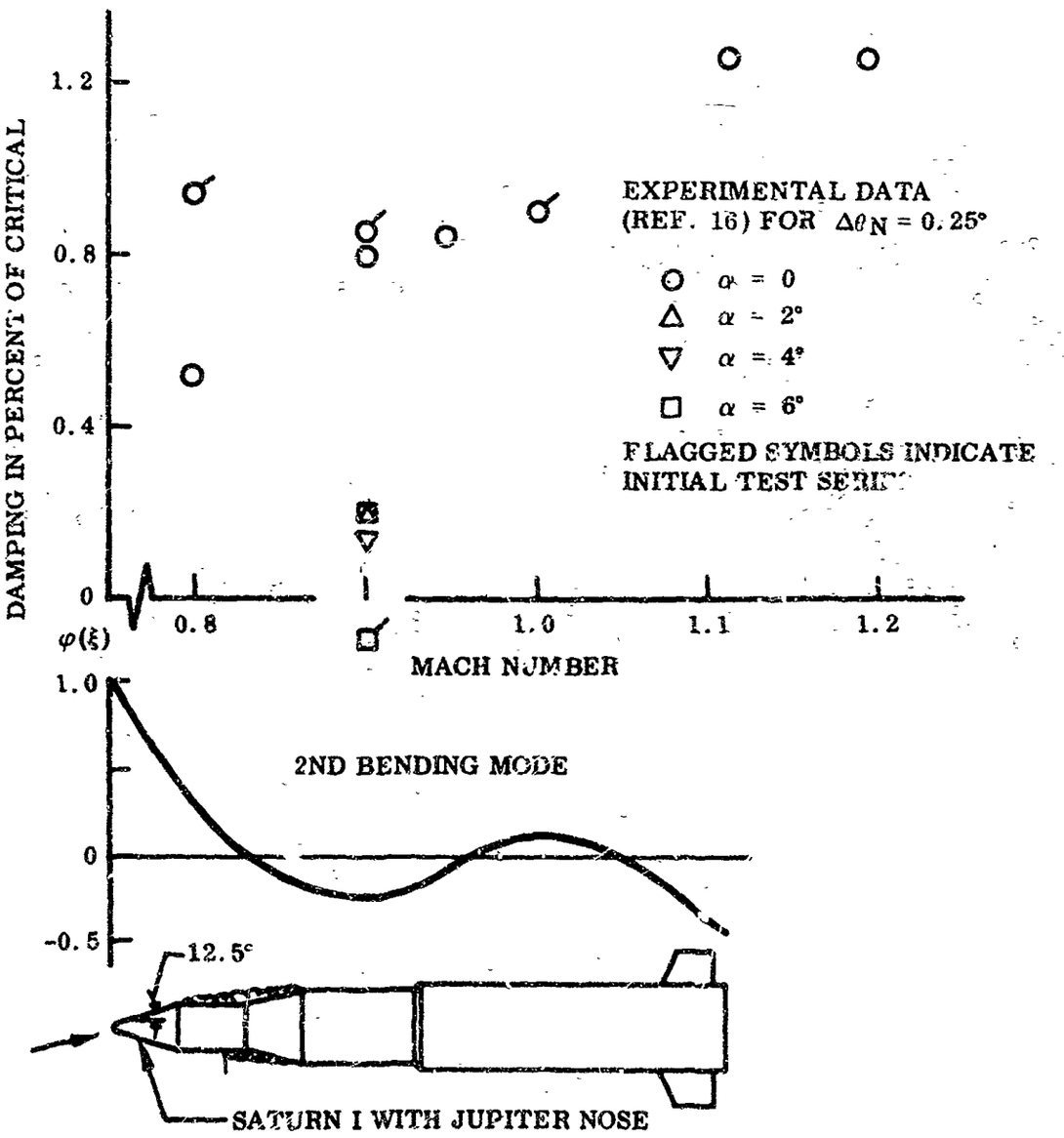
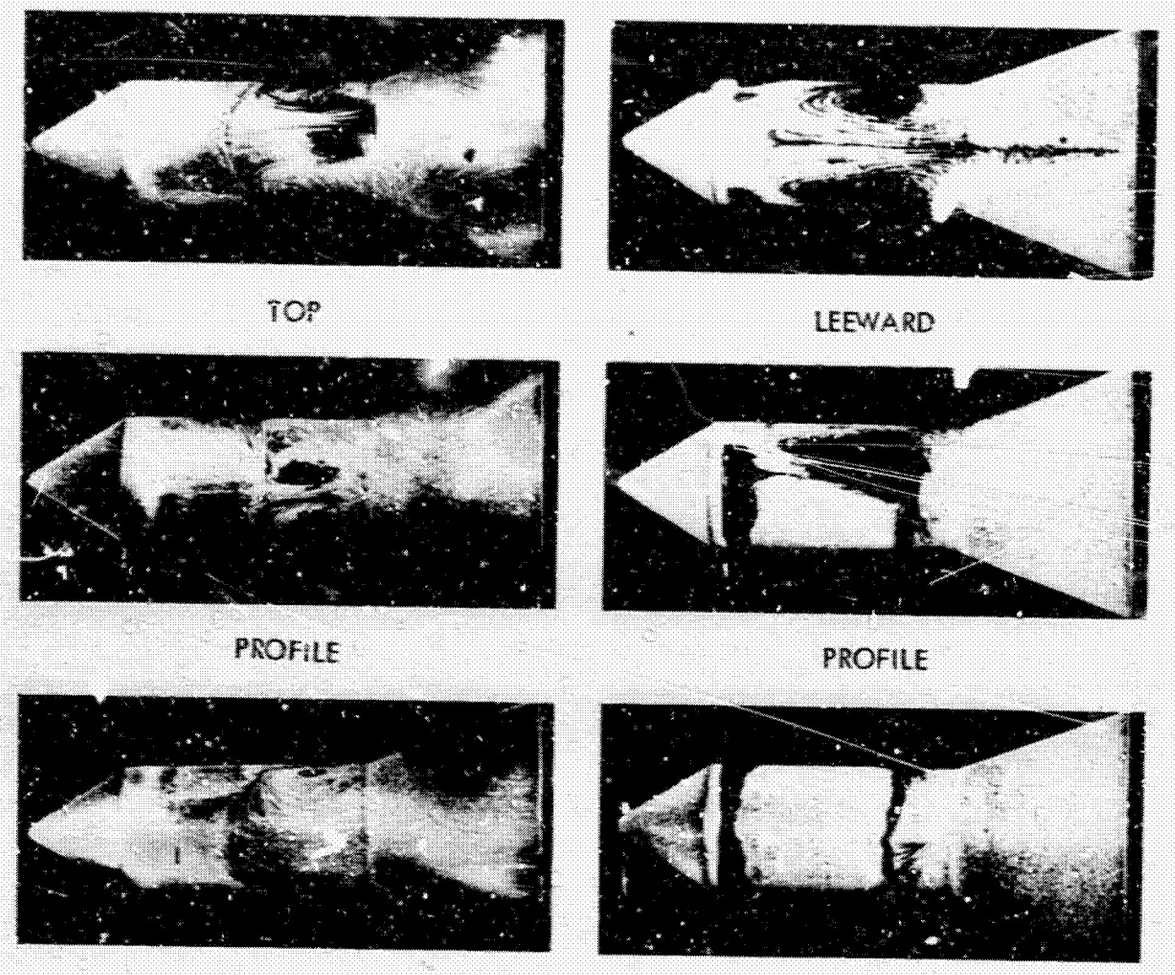


Fig. 9 Aerodynamic Damping Measured on an 8-Percent Elastic Model of Saturn I, Block II Vehicle With a Jupiter Nose



a. $\alpha = 0$

b. $\alpha = 4°$

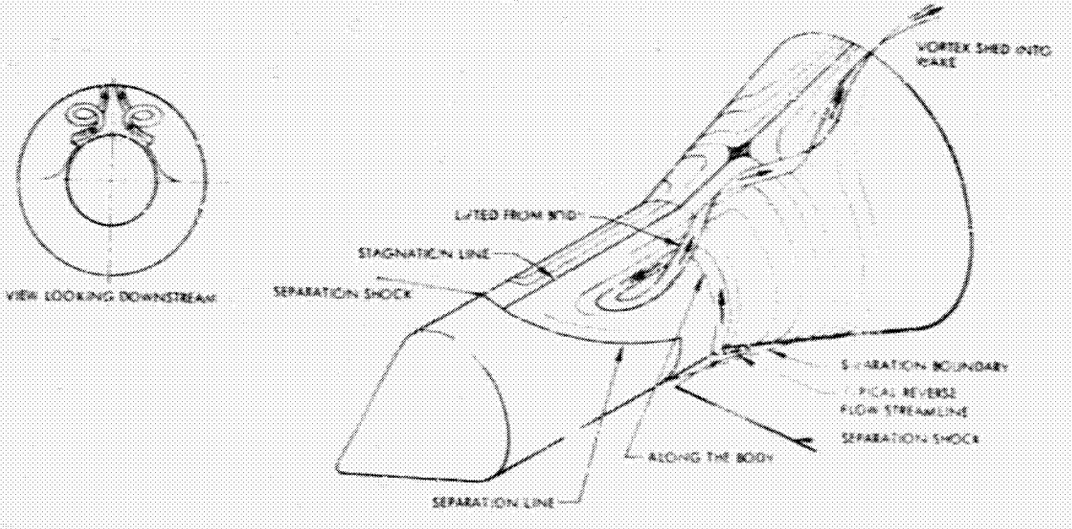


Fig. 10 China Clay Flow Patterns, $\xi_C = 2.0$, $M = 1.2$

the wake over the leeward flare shoulder (see flow sketch inset in Fig. 10). Furthermore, the orientation of the twin vortex pairs at $\alpha = 0°$ were random (compare Figs. 10 and 11). For obvious reasons the flow visualization portion of the test schedule was greatly expanded.

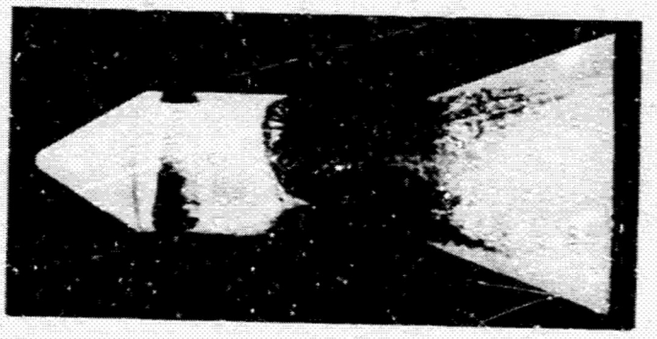
Similar interesting results were obtained for nose-induced separation at M = 0.9. Figure 12 shows that the flow at $\alpha = 0$ over a one-caliber cylinder is not strictly axisymmetric, if one judges from the streamline curvature near the cone shoulder and in the reattachment zone on the flare (Fig. 12a). Pitching the flare causes an inclination of the streamlines in the recirculation region opposite to the flare attitude (Fig. 12b). Thus, the "flipping" of the wake (Refs. 17 and 18) and of the nose-induced separation (Ref. 6) postulated earlier is verified, and a strong upstream communication effect is indicated. Pitching the entire cone-cylinder flare configuration gives a highly curved flow in the recirculation region over the cylinder (Fig. 12c). This flow is reduced by an upward deflection of the flare (Fig. 12d).* For both the angle-of-attack cases and the flare deflection, there is a tendency for the streamlines to converge at the bottom of the cylinder at the cone shoulder. Typical flow visualization photographs of the bottom of the model give no distinct indication of shed vorticity in the plane of the surface (Fig. 13). However, the converging surface streamlines must be vented in some manner (i.e., they indicate a sink). The flow model shown in Fig. 14 is postulated. The separated region is vented through a pair of counter rotating vortices. At higher speeds, when the recirculating mass flow is less, the vortices move aft and out radially, away from the windward meridian, and vorticity in the plane of the surface becomes evident (Fig. 15a). Similarly, for longer cylinders at M = 0.9, the vortices are not confined to the cone shoulder, and vorticity can again be observed on the cylinder aft of the shoulder (Fig. 15b).

When the cylinder length is increased further to $\xi_C = 4.5$, the flow field at M = 0.9 changes considerably. The flow over the cone shoulder is attached, but a local

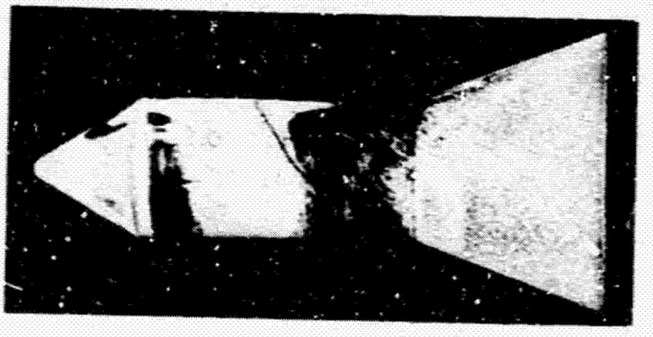
*Two flow visualization techniques are involved here. Figures 12a, 12b, and 12d involve an oil dot technique (Ref. 19), whereas Fig. 12c utilizes a modified china-clay technique. Here the model was sprayed with a mixture of china-clay and oil-of-wintergreen and the resulting flow patterns were photographed. In the former case, the streaking of a series of small oil dots illustrates the flow field.



LEEWARD

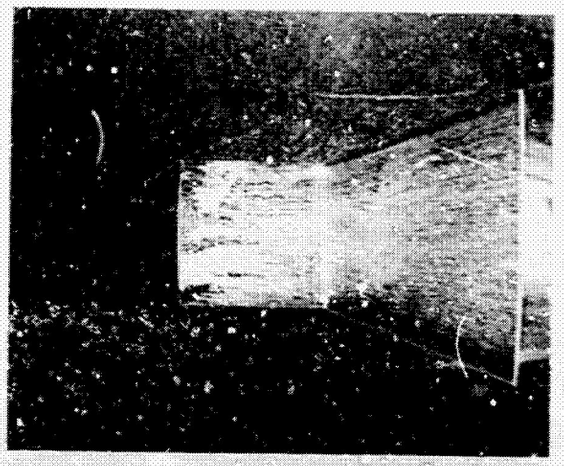


PROFILE

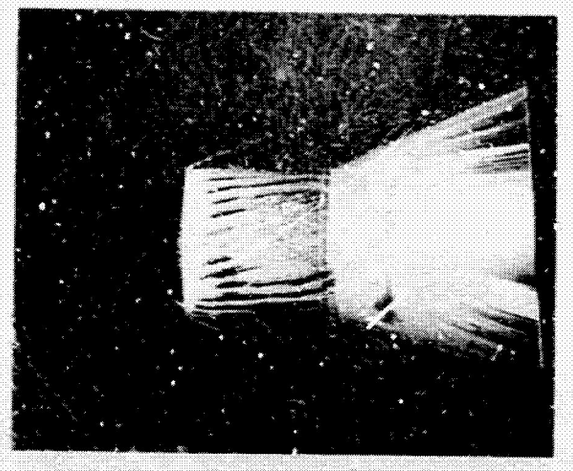


WINDWARD

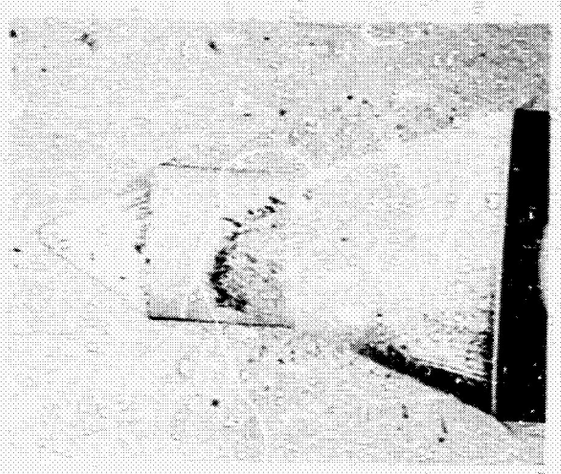
Fig. 11 China Clay Flow Patterns, $\xi_C = 2.0$, $\alpha = 0$, M = 1.2 (Re-run)



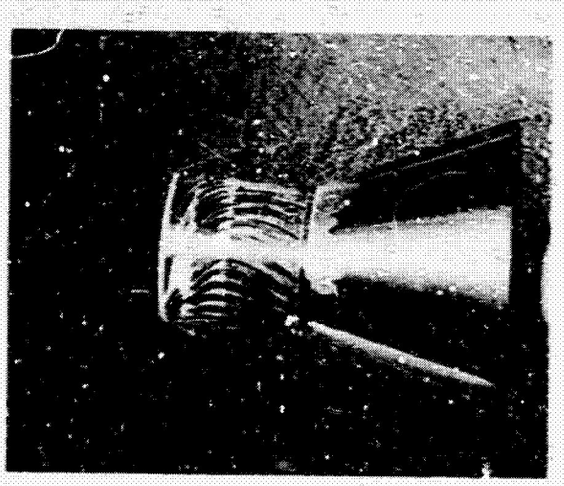
a. $\alpha = 0$, $\delta_F = 0$
(OIL FLOW)



b. $\alpha = 0$, $\delta_F = -4°$
(OIL FLOW)

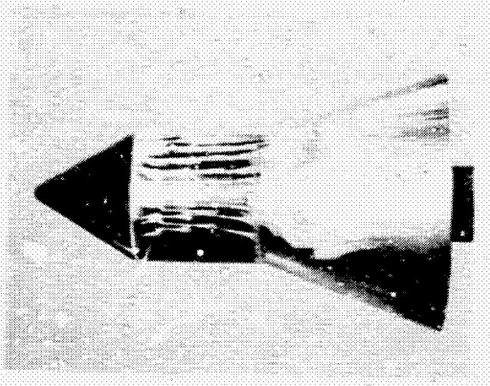


c. $\alpha = 4°$, $\delta_F = 0$
(CHINA CLAY)

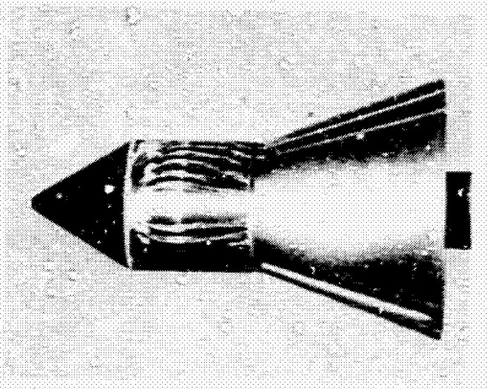


d. $\alpha = 4°$, $\delta_F = -4°$
(OIL FLOW)

Fig. 12 Flow Patterns for Nose-Induced Separation $\xi_C = 1.0$, M = 0.9



$\alpha = 0, \delta_F = -4°$



$\alpha = 4°, \delta_F = -4°$

Fig. 13 Bottom or Windward Side Flow Patterns, $\xi_C = 1.6$, M = 0.9

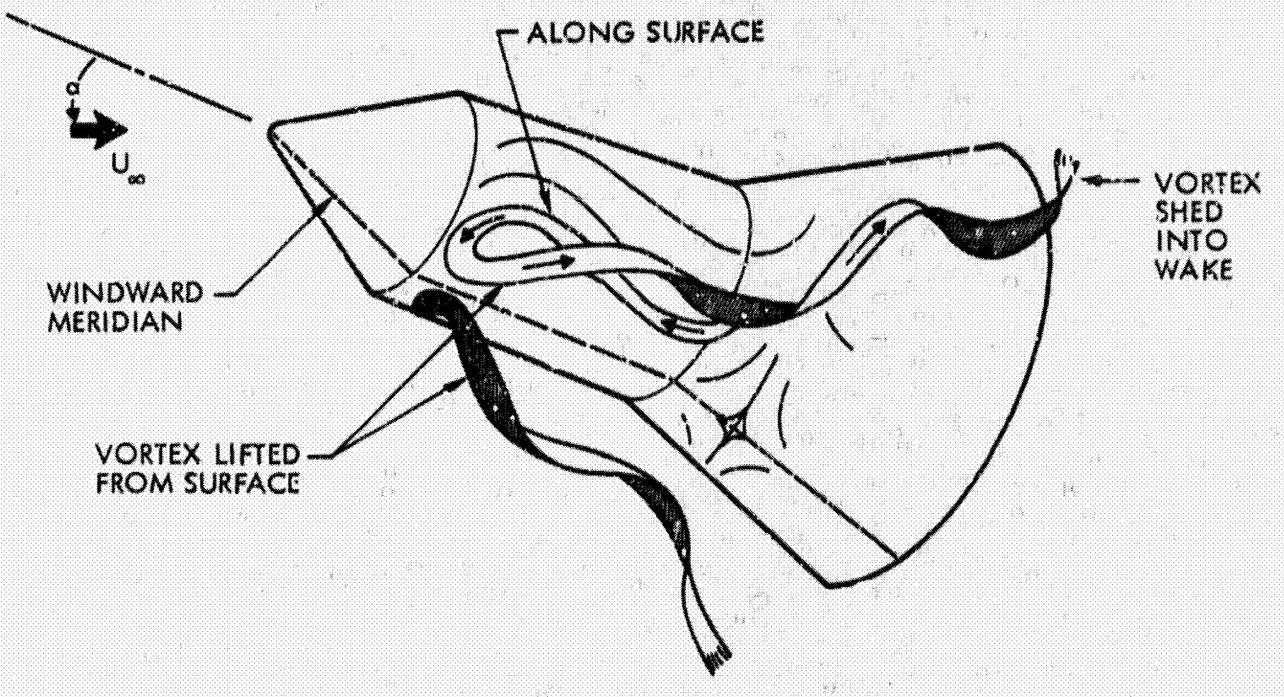
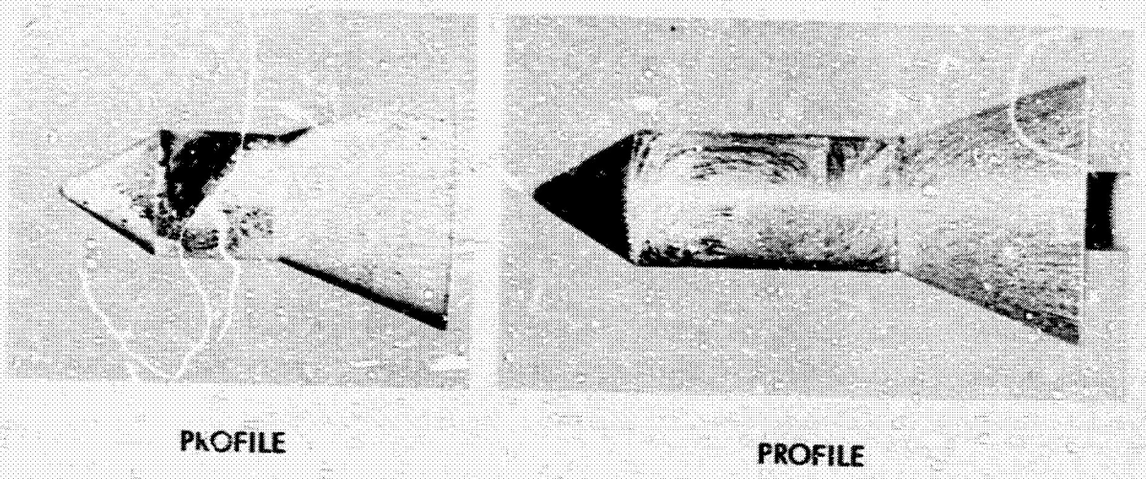


Fig. 14 Flow Model for Nose-Induced Separation



a. $\xi_C = 1.0$, M = 1.2

b. $\xi_C = 2.0$, M = 0.9

Fig. 15 Nose-Induced Separation Windward Vortex Pair, $\alpha = 4°$

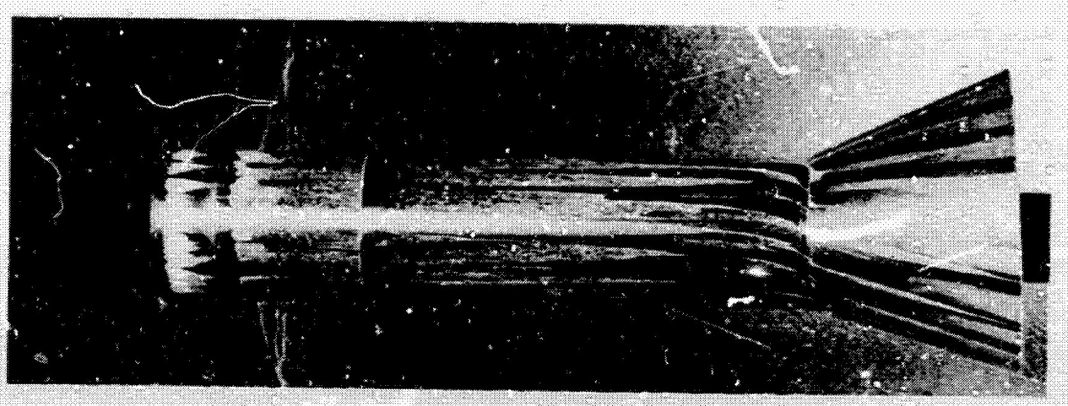
separation is induced by the terminal normal shock (Fig. 16a). This is similar to the shock-induced vortex patterns observed by Chevalier (Ref. 20)*. At angle-of-attack, the leeward-side boundary layer is weakened and the separation jumps to the shoulder, giving the usual nose-induced separation flow field with its large scale vorticity (Fig. 16b). The influence of the flare is restricted to the region just upstream of the flare and does not interact with the nose-induced separated flow region. Thus, upstream communication effects should not be significant at subsonic speeds for long cylinder-flare bodies such as this.

As one would expect, the effect of upstream communication does not vanish for long cylinder-flare bodies when the separation is induced by the flare shock (Fig. 17). Disregarding minor differences for the two cylinder lengths, one finds the flow patterns to be quite similar, with neither giving a definitive indication of the location of the shed vorticity.

The most striking feature of the effect of flare deflection (upwards) on shock-induced separation at $\alpha = 0°$ is illustrated by the correlation between the shadowgraph and the china-clay flow photograph (superimposed in Fig. 17b for the 4.5-caliber cylinder length). The flow near the lateral meridian is turned downward by the slightly skewed flare shock, but does not separate.** The flow along the bottom of the cylinder penetrates the shock without separating until just forward of the flare. Near the leeward meridian, the flow separates in a nearly two-dimensional manner. This recirculating flow along the top surface is pulled down by the unseparated flow along the lateral portions of the cylinder and converges on the bottom cylinder-flare juncture. The flow model shown in Fig. 18 is, therefore, postulated. It essentially describes the flow field seen in the photographs, but proposes a pair of shed vortices (similar to the

*It is possible that the oil dot size (the oil dot technique was used) may affect the scale of the vorticity; however, it does not affect the basic phenomenon (i.e., the vorticies would still be there without oil).

**The shock location may be traced around the body by connecting the locus of points where the streamlines begin to turn.



a. $\alpha = 0°$, $\delta_F = -4°$



b. $\alpha = 4°$, $\delta_F = -4°$

Fig. 16 Effect of Angle-of-Attack on Retarded Separation Flow Patterns, $\xi_C = 4.5$, $M \approx 0.9$

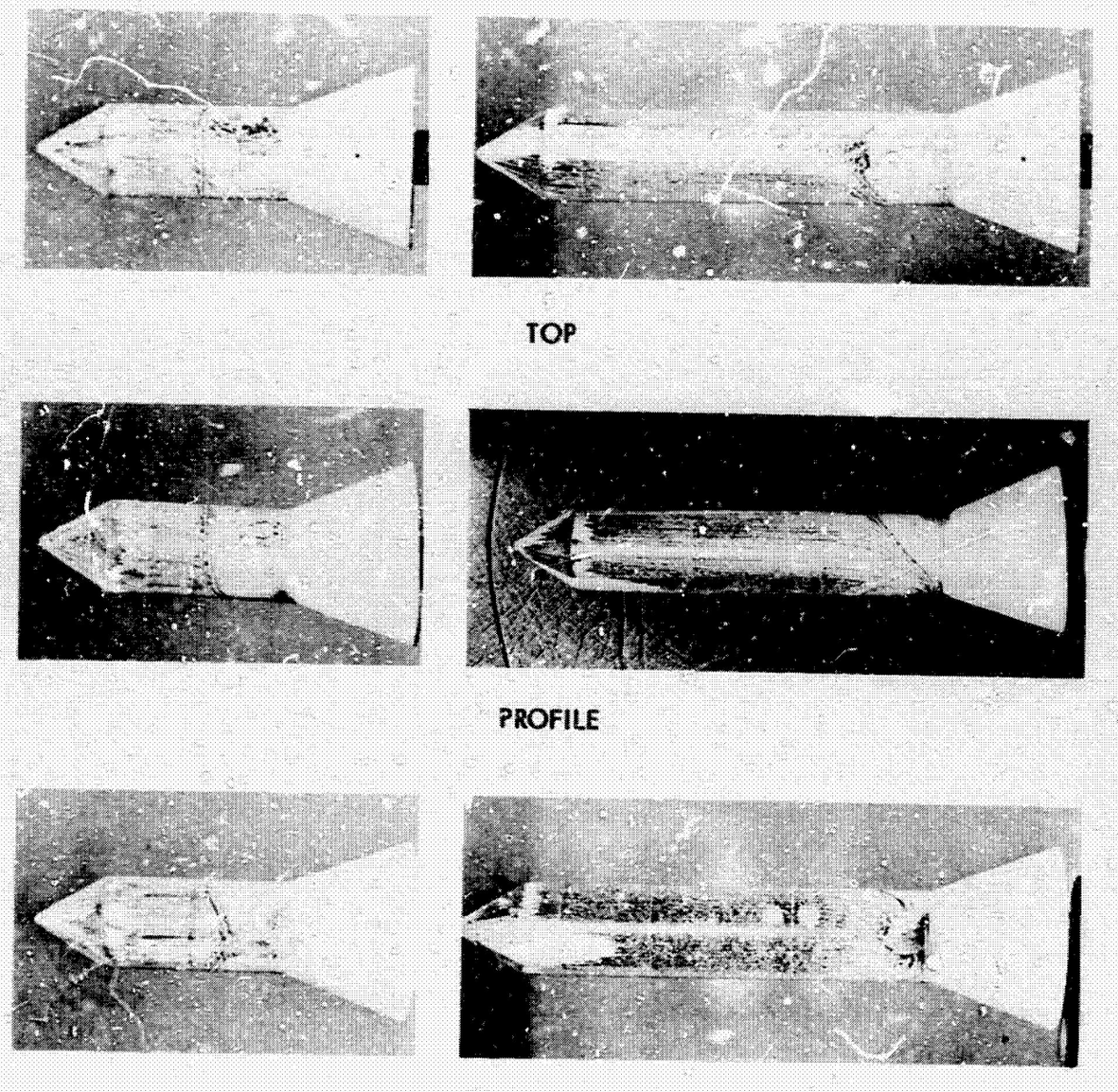


Fig. 17 Shock-Induced Separation Upstream Communication Flow Patterns, M=0.9, α=0°, δ_F=-4°

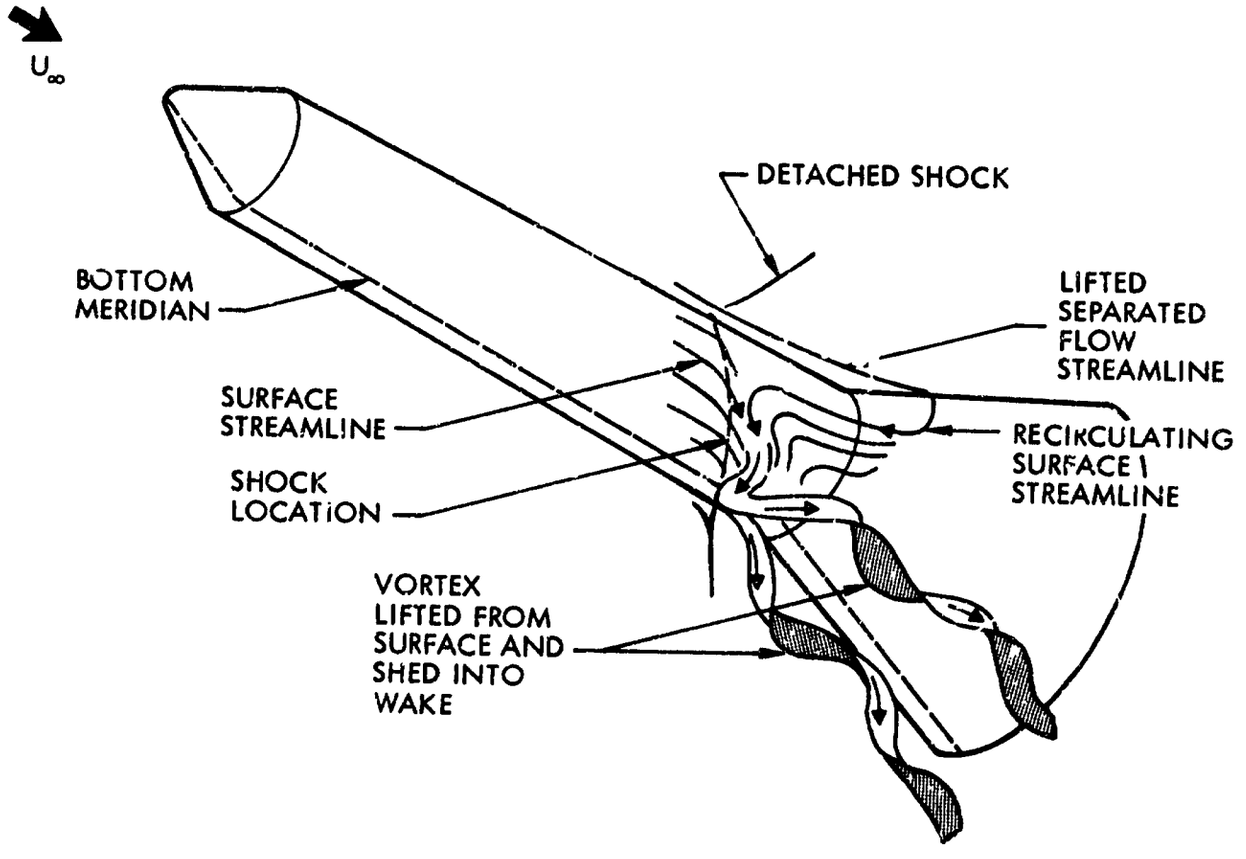


Fig. 18 Shock-Induced Separation Upstream Communication Flow Model, $\alpha = 0$, $\delta_F \neq 0$

model for nose-induced separation on a short cylinder) that vents the flow converging at the bottom cylinder-flare juncture.* The two-caliber cylinder shows very little attached flow aft of the shock (Fig. 17a). This is probably the result of the less energetic transitional boundary layer.

Forebody crossflow dominates the shock-induced separation to an even greater extent than it does nose-induced separation (Figs. 19 and 20). Crossflow thickens and weakens the leeward-side boundary layer by sweeping low energy fluid to the leeward side, and a corresponding strengthening of the windward boundary-layer results. Thus, separation is promoted on the leeward side, resulting in a forward movement and a weakening of the leeward side detached flare shock. The flow photographs (Fig. 19) indicate a large leeward side separation while on the windward side of the flow is attached aft of the shock.** The windward-side flow is then swept to the leeward side (by the transverse pressure gradient resulting from the unequal windward- and leeward-side shock strength) after stagnating at the cylinder-flare juncture. This flow and the recirculating separated flow near the leeward meridian combine to feed large lateral vortices generating essentially the same flow pattern sketched in Fig. 10.

Close examination of Figs. 19 and 20 reveals that the flare, via upstream communication, has a small effect on the flow patterns. That is, the existence of some minor upstream communication effect is indicated. As one would expect, the effect is largest for the shorter cylinder ($\xi_C = 2$) because of its more sensitive transitional boundary layer.

2.4 STATIC AND DYNAMIC MEASUREMENTS

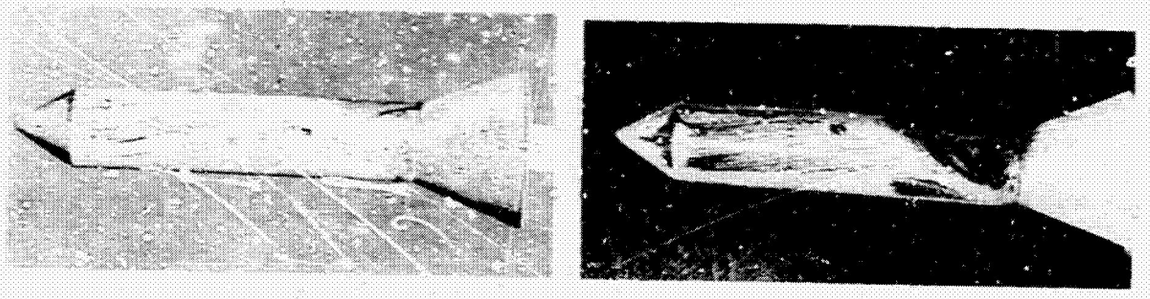
Once one recognizes that the separated flow field is a three-dimensional vortical one, the interpretation of the flare loads becomes more involved (than when one assumes

*The existence of these vortices is indicated by the thick turbulent layer visible on the shadowgraph which correlates with the proposed origin of the vorticity.

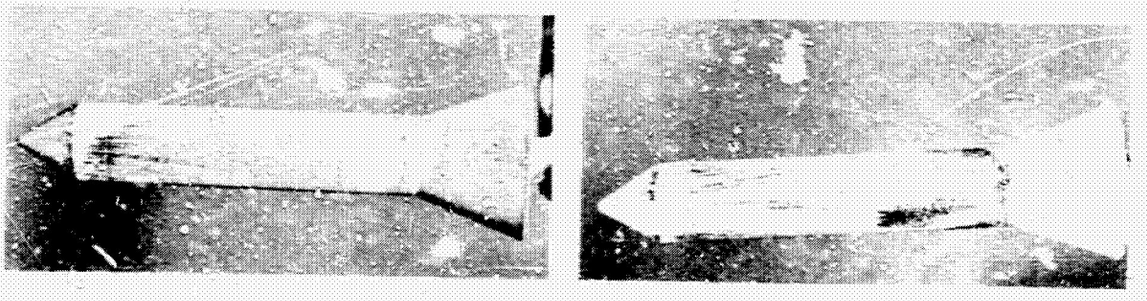
**The vorticity may play a part in energizing and reattaching the windward boundary layer immediately aft of the shock.



LEEWARD



PROFILE

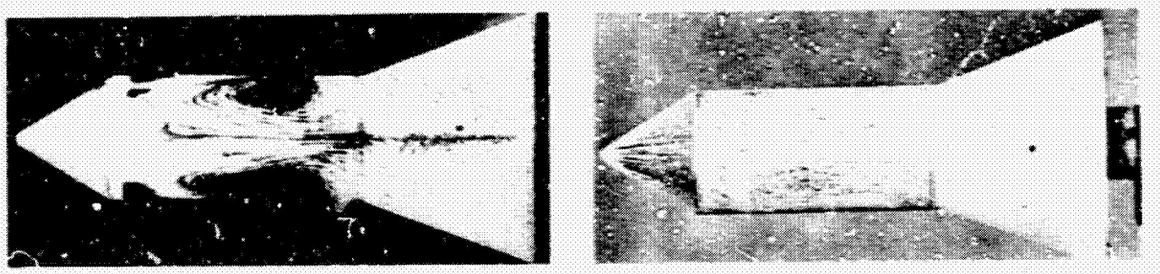


WINDWARD

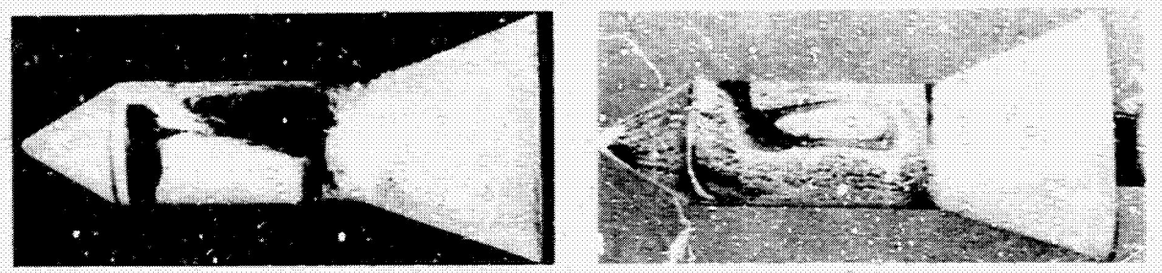
a. $\alpha = 4^{\circ}$, $\delta_F = 0$

b. $\alpha = 4^{\circ}$, $\delta_F = -4^{\circ}$

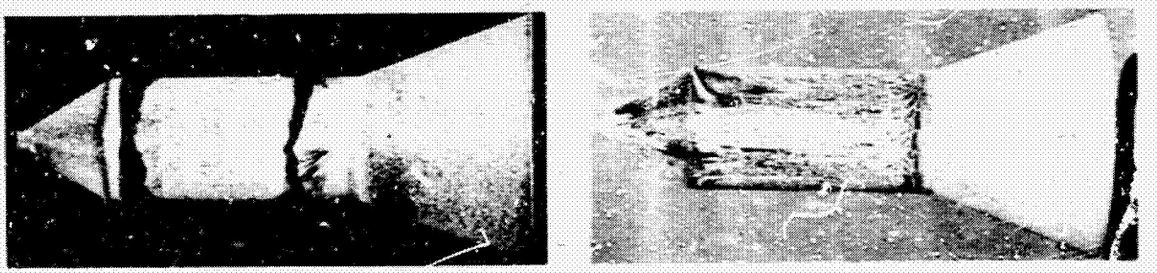
Fig. 19 Effect of Upstream Communication on Shock-Induced Separation Flow Patterns at $\alpha = 4^{\circ}$, M = 1.2, $\xi_C = 4.5$



LEEWARD



PROFILE



WINDWARD

a. $\alpha = 4°$, $\delta_F = 0$ b. $\alpha = 4°$, $\delta_F = -4°$

Fig. 20 Effect of Upstream Communication on Shock-Induced Separated Flow Patterns at $\alpha = 4°$, $M = 1.2$, $\xi_C = 2.0$

axisymmetry). Previously we assumed that the flare load had three components, viz., forebody induced loads (the effect of forebody crossflow), a local load (local crossflow), and the upstream communication load. The local load was assumed to be simply the attached flow load that would be realized without separation, modified to account for the reduced dynamic pressure in the separated region (Ref. 1); i.e.,

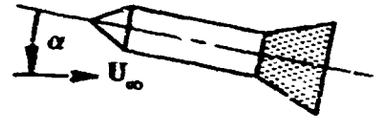
$$C_{N_s} = C_{N_{\alpha_s}} \alpha_s = C_{N_{\alpha_a}} \frac{q_s}{q_a} \alpha_s \tag{1}$$

where

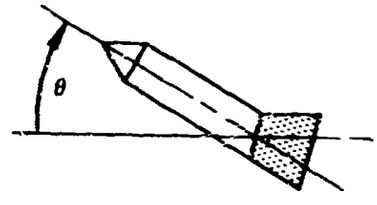
$$\frac{q_s}{q_a} = \frac{C_{A_{o_s}}}{C_{A_{o_a}}}$$

However, if vortices are present in the wake, an additional load increment comes from pitching the flare in the vortex field. Therefore, the data of Ref. 6 were re-examined. The flare loads were measured under three separate conditions:

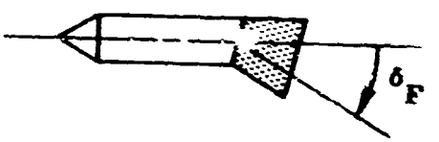
(1) Complete (rigid) body pitching $\left(C_{N_\alpha}\right) \alpha$



(2) Forebody pitching $\left(C_{N_{\theta}}\right) \theta$



(5) Flare deflection $\left(C_{N_{\delta_F}}\right)\delta_F$



The measurements result in the following equations describing the flare loads:

$$C_{N_\alpha}\alpha = C_{N_\theta}\alpha + C_{N_{\alpha_s}}\alpha + C_{N_{\alpha_{V_1}}}\alpha + \Delta^i C_{N_{\alpha_{s_1}}}\alpha \tag{2}$$

$$C_{N_{\delta_F}}\delta_F = C_{N_{\alpha_s}}\delta_F + C_{N_{\alpha_{V_2}}}\delta_F + \Delta^i C_{N_{\alpha_{s_2}}}\delta_F \tag{3}$$

where

C_{N_θ} is measured directly

$C_{N_{\alpha_s}}$ is defined in Eq. (1)

$\Delta^i C_{N_{\alpha_{s_1}}}$ and $\Delta^i C_{N_{s_2}}$ are the upstream communication derivatives

and $C_{N_{\alpha_{V_1}}}$ and $C_{N_{\alpha_{V_2}}}$ are the vortex generated loads

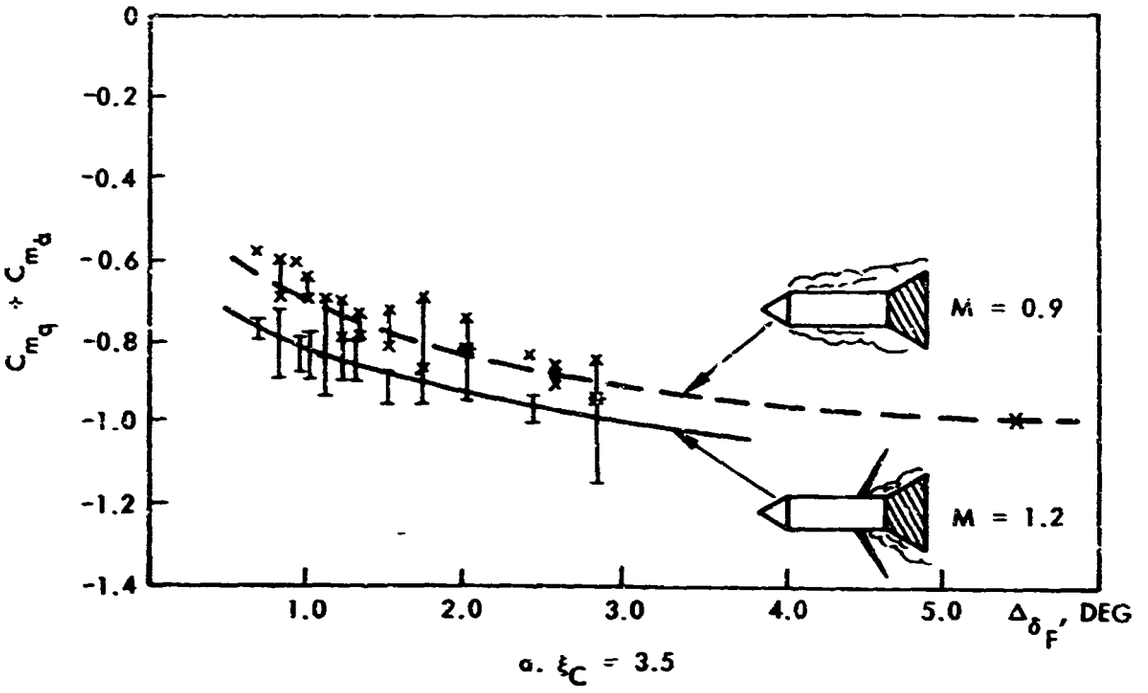
The inequality of the two local vortex loads $\left(C_{N_{\alpha_{V_1}}}\right.$ and $\left.C_{N_{\alpha_{V_2}}}\right)$ and the upstream communication loads $\left(\Delta^i C_{N_{\alpha_{s_1}}}\right.$ and $\left.\Delta^i C_{N_{\alpha_{s_2}}}\right)$ follow from the radically different

vortex patterns at $\alpha = 0$ and $\alpha > 0$. By obtaining free-oscillation pitch-damping measurements of the flare and separate time-lag measurements for the upstream communication effect at $\alpha = 0$, it was hoped that $C_{N_{\alpha_{V_2}}}$ and $\Delta^i C_{N_{\alpha_{s_2}}}$ could be evaluated. The damping introduces an additional unknown, the time lag: hence, separate time lag measurements are needed. Unfortunately, the separate-time lag measurements were unsuccessful. Deflection of the push rod driving the flare caused the flare to pitch about some trim angle-of-attack. As a result, the separation shock did not pass over the transducers during the cycle. (The shock pressures are necessary to get a satisfactory signal to noise ratio.) Consequently, no accurate measurement of the upstream time lag was possible.

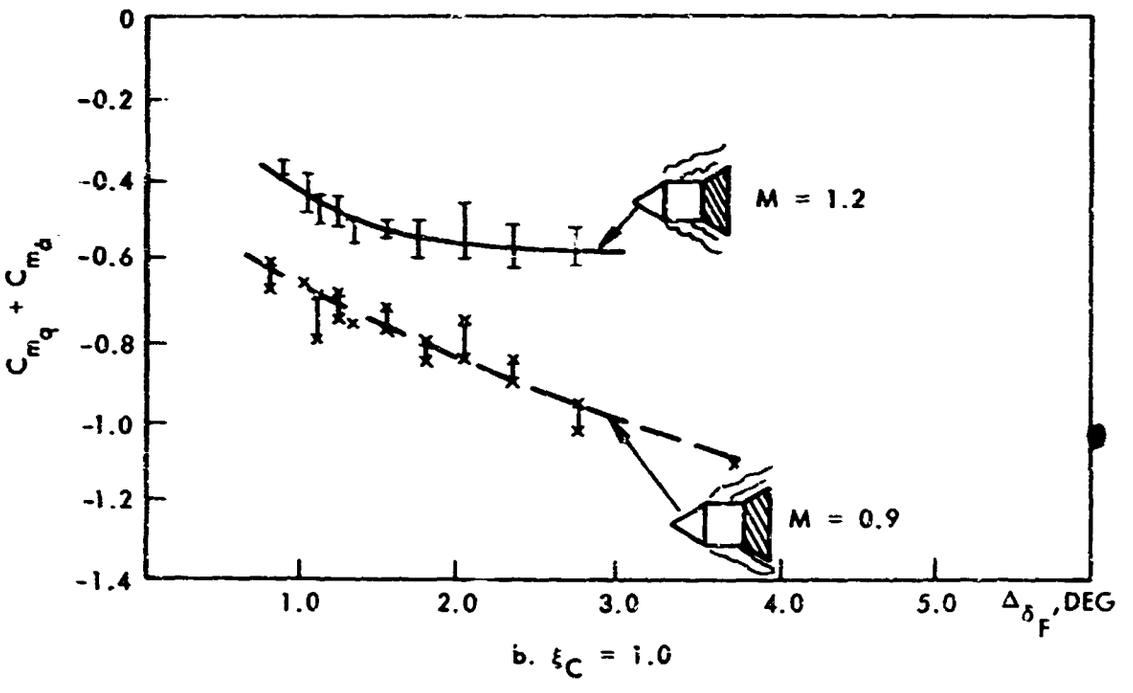
Because of the observed drastic changes in flow patterns, one might expect that the loads induced by pitching the flare could be discontinuous at $\delta_F = 0$. However, the damping results showed only mild nonlinearities and hence tend to preclude the existence of any such discontinuity (Fig. 21 and Refs. 21 and 22).

An attempt was made to correlate the damping results with the previously measured static data using first-order theory. It was assumed that at $\alpha = 3°$ the nonlinear induced loads $\left(\Delta^i C_{N_{\alpha_{s_2}}}\right)$ would be nearly zero: and that one could, as a consequence assume that the flow could be treated as attached, giving proper consideration to the dynamic pressure deficit. The predictions obtained in this manner were in rather poor agreement with experimental data, dynamic as well as static (Fig. 22) In the dynamic test, a discontinuity results at the cylinder-flare juncture (inset sketch in Fig. 22) which could possibly alter the vortex induced effects. Unfortunately, the vortical nature of the flow was not revealed until model design and fabrication had been completed.

Despite the difficulties encountered in the dynamic tests, we believe that the test technique is still potentially effective. Meaningful results could be obtained by rotating the flare about the cylinder-flare juncture: the conditions under which the static loads were obtained could be duplicated after proper redesign of the flare driving system.



a. $\xi_C = 3.5$



b. $\xi_C = 1.0$

Fig. 21 Typical Flare Damping Results

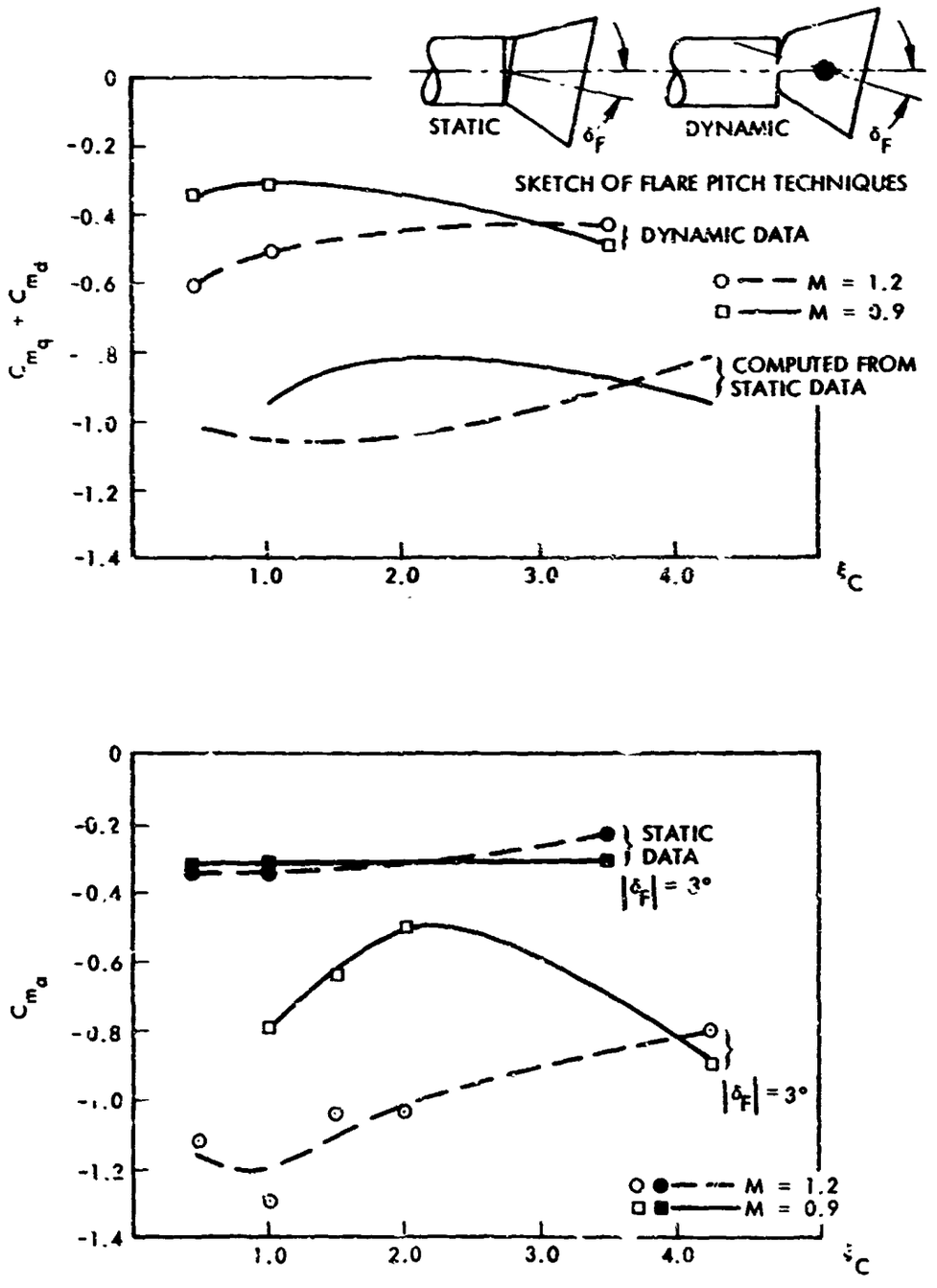


Fig. 22 Comparison of Static and Dynamic Results

2.5 IMPACT ON ELASTIC BODY CALCULATIONS

The drastic change of the vortex patterns with flare attitude (compare Figs. 10 and 17) and angle-of-attack (Fig. 10) suggests that there may be a discontinuous change in the flow field. The static data reveal no discontinuity associated with the load due to forebody cross flow $\left(C_{N_\theta}\right)$. and the damping results give no indication of a discontinuity in $C_{N_{\delta_F}}$. However, the flare loads obtained with and without forebody cross flow, $C_{N_{\alpha_F}}$ and $C_{N_{\delta_F}}$, respectively, are noticeably different, with forebody cross flow consistently giving the larger flare load. $C_{N_{\alpha_F}} > C_{N_{\delta_F}}$ (Figs. 23 and 24).*

There could be a discontinuous load change when the cylinder oscillates through $\alpha = 0$. This stepwise load input could have serious dynamic implications if the flare and forebody cylinder were allowed to oscillate separately i.e., "hinged" at the cylinder-flare juncture. The inapplicability of this to rigid body motion is obvious. Likewise, the elastic body bends continuously. The forebody and the flare will experience continuously distributed cross flow. It therefore appears unlikely that the discontinuity could be of practical concern.

These vortical flow models (Figs. 10, 14, and 18) should not be the source of any great concern in regard to the elastic body dynamics. They do indicate that vortices are shed over the flare shoulder. However, these vortices differ from free body vortices in that they are believed to be contained within the region of viscous flow. Thus, they will not produce coupling between upstream separated regions and downstream body features such as fins. The vortices appear to cause a thickening of the lifted shear layer aft of separation. This is indicated by the considerably thicker shear layer relative to the approaching boundary layer (Fig. 25) and by the sudden thickening of the leeward shear layer at $\alpha > 0$ as crossflow sweeps the lateral vorticies to the leeward side (Figs. 16b and 19b).

---

*The local flare load is also included to give an indication of the relative combined magnitude of vortex dependent $\left(C_{N_{\alpha_V}}\right)$ and upstream communication $\left(\Delta^i C_{N_{\alpha_s}}\right)$ loads. See Eqs. 2 and 3 $\left(C_{N_{\alpha_F}} = C_{N_\alpha} - C_{N_\theta}\right)$.

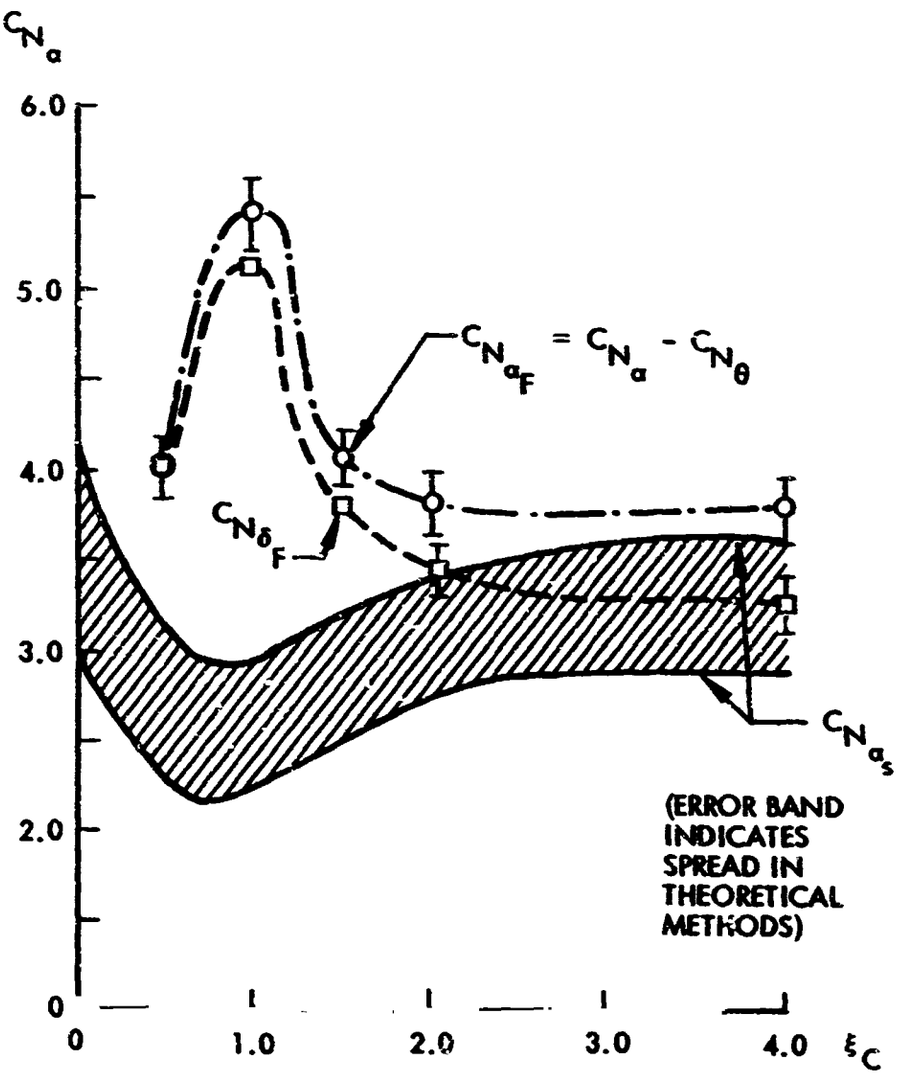


Fig. 23 Flare Normal Force Derivatives at M = 0.9

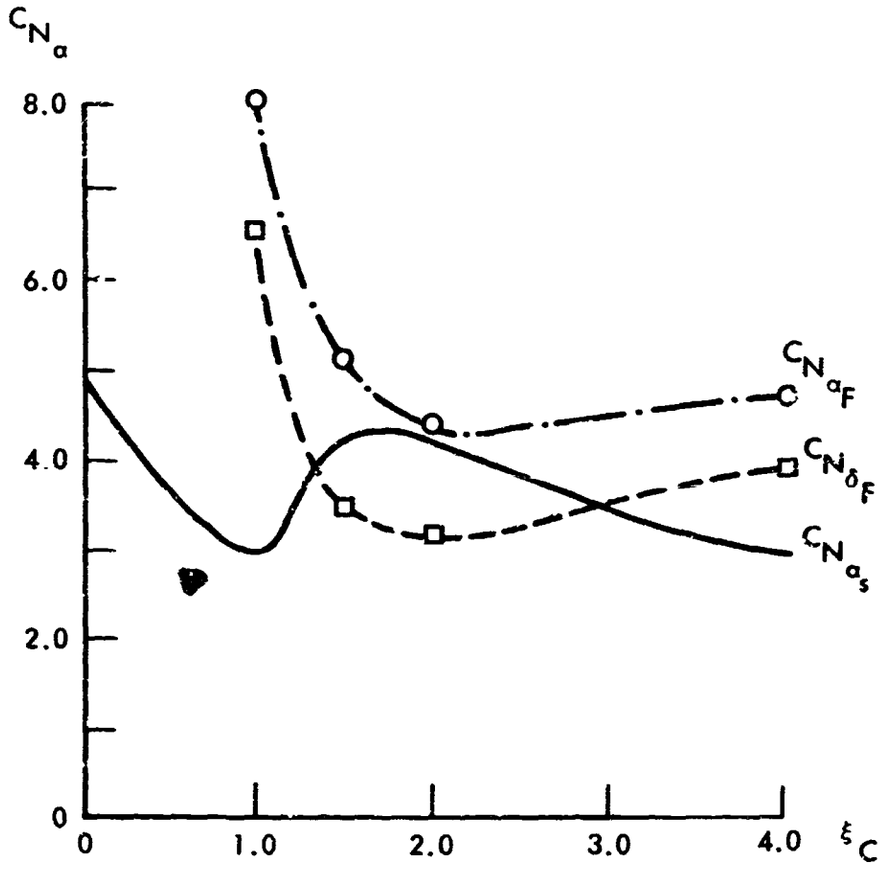


Fig. 24 Flare Normal Force Derivatives at M = 1.2

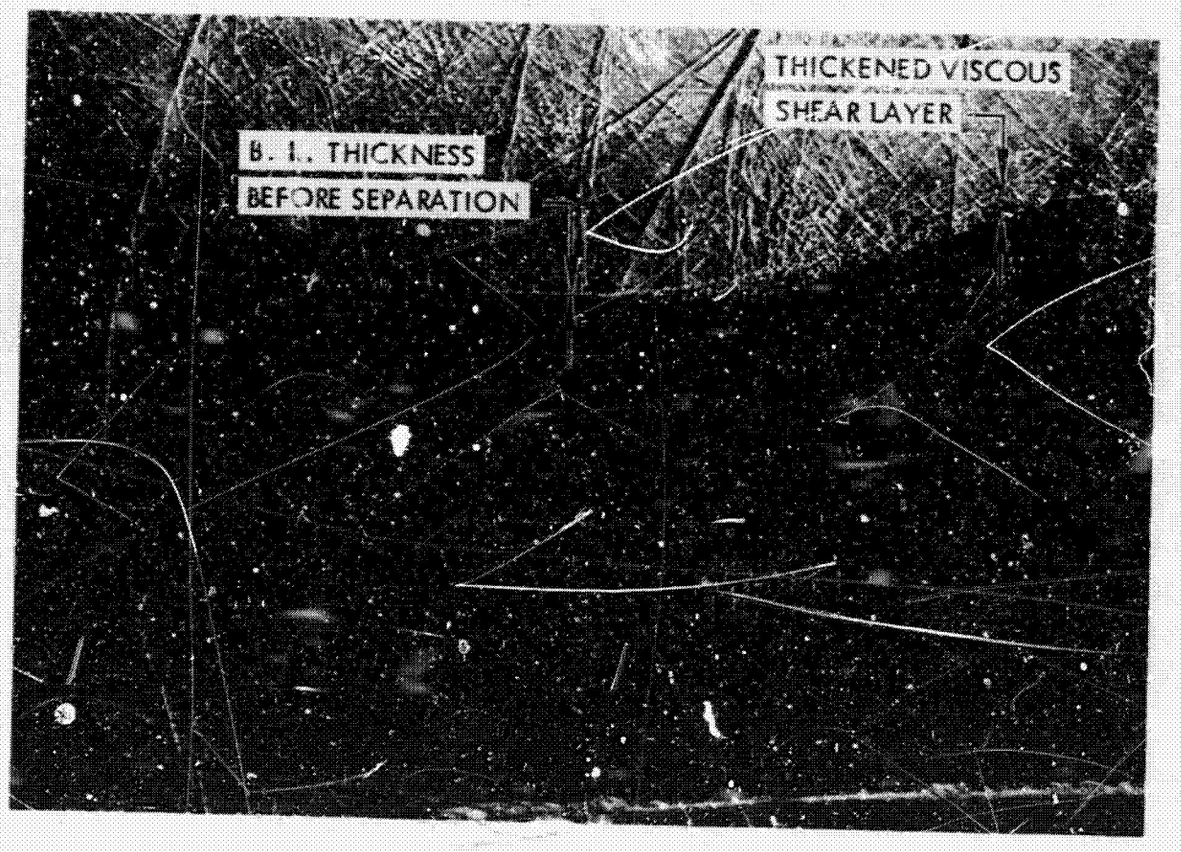


Fig. 23 Effects of Shock-Induced Separation on Thickness of Viscous Layer

This thick shear layer causes the negative shoulder load on aft cylinders (Ref. 1). The vorticity may also cause the thickening of the turbulent boundary layer aft of separated flow regions that has been observed for various Saturn configurations (Ref. 23). However, the thickened boundary layer should not be considered as a mechanism for coupling between adjacent separation regions except when the intervening cylinder is short. The region of direct coupling is probably restricted to about the first 0.5- to 1.0-caliber downstream of the flare (approximate extent of the negative shoulder load). Farther downstream, local crossflow effects begin to dominate and coupling is prevented.

Although the results of the present study seem to pose more problems than they solve, the outlook is not nearly as dismal as it may first appear. First of all, new insight has been gained into the real nature of separated flow. One must certainly recognize its vortical nature before a meaningful theoretical analysis, or even an effective experimental investigation, can be accomplished. Secondly, the flow visualization results have revealed that forebody crossflow dominates the separated flow patterns. Upstream communication effects appear to be of second order (if one judges by their impact on the flow field geometry) relative to forebody crossflow effect. Thus, neglecting upstream communication effects, which to date we have been forced to do out of ignorance, may not be as much in error as was previously feared. However, the large-scale vorticity may explain the difficulty encountered in obtaining meaningful circumferential correlations of fluctuating pressure measurements at or near shock-induced separations.

Section 3
CONCLUSIONS

Present theoretical techniques treat shock-induced separation as an axisymmetric flow. But results obtained in this investigation have indicated that the flow field is vortical. Thus, all existing theoretical results will have to be reevaluated in that light.

The experimental results tend to verify the concept that the (escape rocket) wake and the nose-induced separation are being "flipped" by a submerged conic body as the result of upstream communication. Furthermore, they indicate that forebody crossflow tends to dominate the separation by drastically changing the vortex configurations, thus minimizing the impact of upstream communication. Based on this qualitative information, it appears that neglecting upstream communication effects may in many cases be a reasonable assumption in the quasi-steady computations of the aerodynamic damping of elastic bodies. To support such an assumption, conclusive quantitative information is obviously needed.

Section 4
RECOMMENDATION FOR FUTURE STUDY

The present study drastically affects all previous conceptions of shock-induced separation. Certainly, more basic information is needed for a thorough understanding of shock-induced separation. Also desirable is detailed mapping of the vortices, their induced pressure field, and their variation with body geometry, Reynolds number, Mach number, and tunnel turbulence level. Furthermore, with improved push rod design a direct measurement of the upstream time lag still may be possible from phase lag measurements of the shock oscillations driven by an oscillating flare.

Of primary concern is the application of the separation-induced loads to elastic body dynamics, specifically to the Saturn V. Thus, any further study of shock-induced separation should include the following items.

(1) Literature search and theoretical investigation of vortices and their induced pressures making use of the latest information obtained through flow visualization

(2) Flow visualization study on the forward portion of Saturn V-Apollo vehicle (including S-4B-SII interstage frustum) to discover any unusual flow features that might result from the numerous regions of reattaching and reseparating flow

(3) Flow visualization study to investigate the effects of various geometric and flow field parameters on the vorticity

(4) Continuation of presently unsuccessful attempt to measure upstream time lag in regions of shock-induced separation with an improved mechanical design

(5) Detailed static and limited fluctuating pressure survey of external and body surface flow fields to map vortex positions and induced static and fluctuating pressures (with special emphasis on the Saturn V-Apollo configuration)

PRECEDING PAGE BLANK NOT FILMED.

The study outlined above will result in a better basic understanding of the shock-induced separated flow field, and will define once and for all the importance of upstream communication effects on the elastic body dynamics. It would also lay the foundation for a better understanding of the buffet input, i.e., the fluctuating pressure field in regions of shock-induced boundary-layer separation.

Section 5
REFERENCES

1. L. E. Ericsson and J. Peter Reding, "Analysis of Flow Separation Effects on the Dyanmics of a Large Space Booster", J. Spacecraft and Rockets, Vol. 2, No. 4. Jul–Aug, 1965, pp. 481–490

2. Lockheed Missiles & Space Company, Dynamics of Separated Flow Over Blunt Bodies, by L. E. Ericsson and J. Peter Reding. Technical Summary Report 2-80-65-1, Contract NAS 8-5338, Sunnyvale, Calif., Dec 1965

3. A. Gerald Rainey, "Progress on the Launch Vehicle Buffeting Problem," J. Spacecraft and Rockets, Vol. 2, No. 3. May–Jun 1965, pp. 289–299

4. Lockheed Missiles & Space Company, Aerodynamic Characteristics of Saturn 1B and Saturn V Launch Vehicles, by L. E. Ericsson and J. Peter Reding. Technical Summary Report M-37-67-5, Contract NAS 8-11238, Sunnyvale, Calif., Dec 1967

5. -----, Flow Separation Studies, by R. A. Guenther, Technical Report L-87-66-1, Contract NAS 8-20354, Sunnyvale, Calif., Dec 1966

6. -----, Preliminary Experimental Investigation of Separated Flow Loads on Cone-Cylinder-Flare Bodies, by R. A. Guenther and J. Peter Reding, Technical Report L-87-67-1, Contract NAS 8-20354, Sunnyvale, Calif., Feb 1967

7. -----, Steady and Unsteady Terminal Shock Aerodynamics on Cone-Cylinder Bodies, by L. E. Ericsson, Technical Report L-87-67-2, Contract NAS 8-20354, Sunnyvale, Calif., Oct 1967

8. -----, The Aeroelastic Characteristics of the Saturn 1B Launch Vehicle With Biconic Payload Shroud, by L. E. Ericsson, N. J. French, and R. A. Guenther, Technical Report M-37-67-1, Contract NAS 8-11238, Sunnyvale, Calif., Jul 1967

9. -----, Computer Program for Quasi-Steady Aero-Elastic Analysis, by Nancy L. Davis, LMSC M-37-67-3, Contract NAS 8-11238, Dec 1967

10. David Needham and John J. Stollery, "Boundary Layer Separation in Hypersonic Flow," AIAA Paper No. 66-455, 27-29 Jun 1966

11. National Advisory Committee for Aeronautics, Investigation of Separated Flow in Supersonic and Subsonic Streams With Emphasis on the Effect of Transition, by D. R. Chapman, D. M. Kuehn, and H. K. Larson, NACA TN-3869, Mar 1957

12. L. Trilling, "Oscillating Shock Boundary Layer Interaction," J. Aeronaut. Sciences, Vol. 25, No. 5, May 1958, pp. 301-304

13. Arnold Engineering Development Center, Characteristics of Steady-State Pressures on the Cylindrical Portion of Cone-Cylinder Bodies at Transonic Speeds, by J. E. Robertson and H. L. Chevalier, AEDC TDR 63-104, Aug 1963

14. National Advisory Committee for Aeronautics, A Second-Order Shock-Expansion Method Applicable to Bodies of Revolution Near Zero Lift, by C. A. Syvertson and D. H. Dennis, NACA Report 1328, 1957

15. C. F. Coe, NASA Ames Research Center, private communication of currently unpublished data

16. National Aeronautics and Space Administration, Aerodynamic Damping and Buffet Response of an Aeroelastic Model of the Saturn I Block II Launch Vehicle, by P. W. Hanson and R. V. Doggett, Jr., NASA TN D-2713, Mar 1965

17. Lockheed Missiles & Space Company, Forces Induced on Bodies in Free Wakes and Three-Dimensional Cavities, by J. P. Reding, LMSC-667990, Contract NAS 8-5338, Sunnyvale, Calif., Dec 1965

18. J. P. Reding and L. E. Ericsson, "Loads on Bodies in Wakes," J. Spacecraft and Rockets, Vol. 4, No. 4, 1967, pp. 511-518

19. National Research Council of Canada, A Note on a Technique of Surface Flow Visualization, by R. F. Meyer, Aero. Report LR-457, Ottawa, Canada, Jul 1966

20. H. L. Chevalier, NASA Ames Research Center, private communication of currently unpublished data.

21. Lockheed Missiles & Space Company, Experimental Evaluation of The Upstream Communication Time and Dynamic Stability of the Aft Flare for Shock-Induced and Hammerhead Configurations, by R. A. Lott and P. T. Johnson, LMSC/HREC D148695, Huntsville, Ala., Feb 1969

22. -----. Additional Results of Dynamic Stability Testing of Shock-Induced Separation Model, by P. T. Johnson, LMSC/HREC D148753, Huntsville, Ala., Feb 1969

23. NASA George C. Marshall Spaceflight Center, Shadowgraph Study of the Upper Stage Flow Fields of Some Saturn V Study Configurations in the Transonic Mach Number Range, by C. Dale Andrews and David R. Carlson, Internal Note R-AERO-IN-47-63, Nov 29, 1963

24. National Aeronautics & Space Administration, The Interaction of an Oblique Shock Wave With a Laminar Boundary Layer, by R. J. Hakkinen, I. Greber, L. Trilling, and S. S. Abarbanel, Memo 2-18-59W, Mar 1959

25. Thomas, B. K. Jr., "NASA Evaluating Apollo Changes," Aviation Week and Space Technology, May 13, 1968 pp. 95–97

26. Aviation Week and Space Technology, Apr 15, 1968, p. 29

Appendix A
NOMENCLATURE

Variables and Constants

a	speed of sound, m/sec
A	forebody axial force, kg. coefficient $C_A = A/(\rho U^2/2)S$
c	reference length or cylinder caliber, m
c_f	local friction coefficient (Fig. 2)
H	total pressure, kg/m^2
h	height of dividing stream line, m
L_C	cylinder length, m
L_{sep}	separated flow extent, m
M	Mach number (U/a)
N	normal force, kg [coefficient $C_N = N/(\rho U^2/2)S$]
p	static pressure, kg/m^2 [coefficient $C_p = (p - p_\infty)/(\rho U^2/2)$]
P	static pressure ratio, $P = (p - p)_\infty/H_\infty$
q	dynamic pressure, kg/m^2 ($q = \rho U^2/2$)
R_c, R_{x_o}	Reynolds number, $R_c = U_\infty c/\nu_\infty$; $R_{x_o} = U_e x_o/\nu_e$
S	reference area, $\pi c^2/4$
u	x-component of local velocity, m/sec
$\bar{u}$	average back flow velocity, m/sec
U	vehicle velocity, m/sec
v	y-component of local velocity, m/sec

PRECEDING PAGE BLANK NOT FILMED

v	crossflow, m/sec
x	axial coordinate, m
x_o	boundary layer approach length, m (Figs. 1 and 2)
y	vertical or radial coordinate, m
α	angle-of-attack, radian or deg
δ	boundary-layer thickness, m
δ_F	flare attitude, radian or deg
Δ	incremental difference
θ	cylinder attitude. radian or deg
θ_c	cone half angle. radian or deg
θ_w	wedge or flap angle, radian or deg
ν	kinematic viscosity, m^2/sec
ξ	dimensionless axial coordinate, $\xi = x/c$ and $\xi_C = L_C/c$
ρ	density of air, kg sec^2/m^4

Subscripts

a	attached flow
B.L.	due to boundary-layer buildup
c	cone
crit	critical
C	cylinder
D	dividing streamline
e	local external flow
K	flap or ramp
o	at $\xi = 0$ or $\alpha = 0$
p	plateau

δ	due to pressure gradient buildup (δ = constant)
R	reattachment
s	separated flow
V	vortex
W	wedge or flap
1	rigid body mode
2	flare deflection mode
3,4	numbering subscripts (Fig. 1)
∞	undisturbed flow

Superscripts

i	induced, e.g., $\Delta^i C_{N_s}$ = separation-induced normal force coefficient

Differential Symbols

$$P_\xi = \frac{\partial P}{\partial \xi}$$

$$C_{N_\alpha} = \frac{dC_N}{d\alpha} \quad , \quad C_{N_\theta} = \frac{\partial C_N}{\partial \theta} \qquad C_{N_{\delta_F}} = \frac{\partial C_N}{\partial \delta_F}$$

$$\left(\frac{\partial C_N}{\partial \alpha}\right)_\delta = \frac{\partial C_N}{\partial \alpha} \text{ at } \delta = \text{constant}$$

$$\left(\frac{d\Delta^i \xi_s}{d\alpha}\right)_{B.L.} = \frac{d\Delta^i \xi_s}{d\alpha} \text{ at constant inviscid pressure gradient}$$

Appendix B

SELF-SUSTAINED SHOCK OSCILLATIONS

A simplified theoretical model of two-dimensional, steady boundary-layer separation was extended to include time-dependent perturbation in the reattachment region caused by an oscillating flap. The analysis was similar to that of Trilling (Ref. 12) in deriving the viscous flow parameters but differed in the treatment of the external inviscid flow. It was hoped that this analysis could be extended with some modifications to bodies of revolution. However, this extension breaks down when one considers the existence of vortical flow in the recirculating region. At present it is uncertain that there are any local truly two-dimensional flow pockets in flow over bodies of revolution where this analysis would be applicable.

Inherent in the assumption of a two-dimensional flow pocket is the Chapman-type cross section of a separated boundary layer sketched in Fig. B-1.

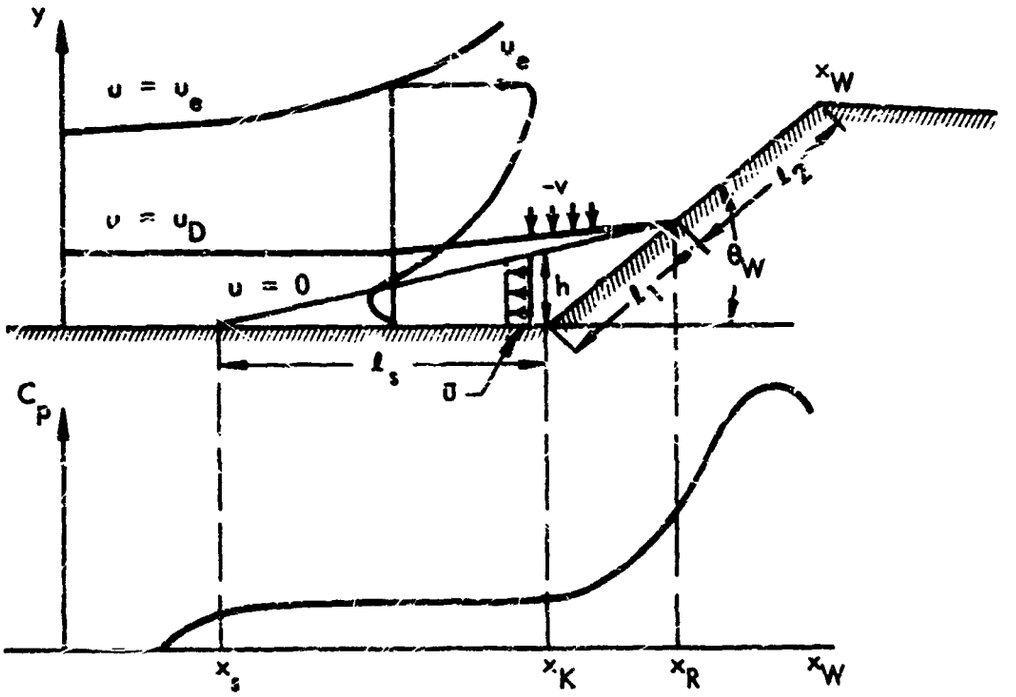


Fig. B-1 Separated Flow Profiles and Pressure Distribution in a Compression Corner

PRECEDING PAGE BLANK NOT FILMED

The assumption of small, time-dependent perturbations from the steady state condition allows one to simplify the x-momentum equation.

$$\rho u \frac{\partial u}{\partial x} + \rho v \frac{\partial u}{\partial y} + \frac{\partial p}{\partial x} = \frac{\partial}{\partial y}\left(u \frac{\partial u}{\partial y}\right) \tag{B.1}$$

Along the $u = 0$ line the shear force is assumed to be relatively constant*; therefore one may conclude that:

$$\rho v \left.\frac{\partial u}{\partial y}\right|_{ave.} = - \frac{\partial p}{\partial x} \tag{B.2}$$

Replacing ρv from the continuity equation and integrating Eq. (B.2) in x, one obtains:

$$\frac{|\bar{u}|}{u_e} = \frac{\Delta C_{p_R}}{c_{f_{ave}}} \Bigg/ R_{x_K}\left(\frac{h}{x_K - x_0}\right) \quad ; \quad R_{x_K} = \frac{(x_K - x_0)\, u_e}{\nu} \tag{B.3}$$

where

ν = kinematic viscosity

ΔC_{p_R} = pressure coefficient change from x_K to x_R

$c_{f_{ave}}$ = average friction coefficient at $u = 0$ line

h = height of $u = 0$ line at x_K

x_K = location of the flare cylinder juncture

x_0 = effective approach length for boundary layer being separated

*Hakkinen et al. (Ref. 24) have shown that for shock-induced separation, the term $(\mu u_y)_y$ is small compared to the remaining quantities in the momentum equation.

The back flow velocity is perturbed about its equilibrium value to determine the relationship between the perturbations of the other parameters in the problem. It was assumed that changes in the other components were either instantaneous or lagged the initial disturbance by a finite time, Δt. To determine if self-sustained oscillations can exist, the "critical" conditions were found at which the oscillations would continue even if the forcing function were removed. Forces and moments were examined to see if residual forces and moments persisted after the purely forced term was deleted. To obtain a workable equation, it was assumed that the pressure acted over well-defined areas; e.g., the plateau pressure was effective up to the instantaneous reattachment point. The incremental force and the incremental moment around x_K thus become:

$$\Delta F = \Delta x_R(t;t+\Delta t)\,[p_R(t;t+\Delta t) - p_p(t+\Delta t)] - (x_R' - x_K)\,[p_p - p_p(t+\Delta t)] + [(x_W - x_R')(p_W - p_W(t))] \qquad (B.3)$$

$$\Delta M = (x_R' - x_K)\,\Delta x_R(t;t+\Delta t)\,[p_R(t;t+\Delta t) - p_p(t+\Delta t)] - (x_R' - x_K)^2\,[p_p - p_p(t+\Delta t)] + (x_W - x_R')(x_W + x_R' - 2x_K)\,[p_W - p_W(t)]/2$$

where the subscripts are defined as follows:

- R = reattachment
- p = plateau
- K = flat plate corner
- W = flap after reattachment
- Δx_R = the movement of the reattachment point

The position x_R' is defined as the instantaneous position of the reattachment point. It differs from the mean reattachment position by $\Delta x_R(t;t+\Delta t)$. Since the increment is a first-order term and the pressure increments are also first-order terms, the product is of second order and can be ignored in Eqs. (B.4). Therefore, in the remaining development x_R' will be replaced by its mean value x_R.

The normalized pressures can be determined from the small wedge angle approximation for supersonic flow. Expanding this solution in a Taylor series for small perturbations about the initial values, one obtains:

$$\Delta p = (p - p_\infty)\left[\frac{\Delta\theta}{\theta} - \frac{M\Delta M}{\left(M^2 - 1\right)}\right] \tag{B.5}$$

One may now substitute into Eq. (B.4) the appropriate expressions for the Δp's.

For unsteady motion of a body in a supersonic flow field, one must consider both the instantaneous and the downwash apparent angle of turning to compute the total force on the flap. Thus, the apparent instantaneous angle of the flap is:

$$\theta(t) = \theta_0 + \Delta\theta(t) + \Delta\dot{\theta}(t)\,\ell/u_e \tag{B.6}$$

The angle θ_0 is the mean angle, $\Delta\theta(t)$ is the actual instantaneous position of the flap relative to the mean position, and $\Delta\dot{\theta}(t)\,\ell/u_e$ is the downwash angular change of the flow due to the moving flap. For quantities which vary with the time lag, one may expand the expression to obtain:

$$\theta(t + \Delta t) = \theta_0 + \Delta\theta(t) + \Delta\dot{\theta}(t)\,\ell/u_e + \Delta\ddot{\theta}(t)\,\ell/u_e \tag{B.7}$$

The last term in (B.7) is the accelerated flow effect and will be ignored to remain consistent with the initial assumptions.

If one expands Eq. (B.4), in time, one obtains the following system of equations:

$$\Delta M = \ell_s(p_R - p_p)\left[\Delta x_{R_1}(t) + \Delta x_{R_2}(t) + \Delta\dot{x}_{R_2}(t)\,\Delta t\right] - \ell_s^2(p_p - p_1)\left[\Delta p_p(t) + \Delta\dot{p}_p(t)\,\Delta t\right]/2 + (\ell_1 + \ell_2)\,\ell_2\,(p_W - p_1)\,\Delta p_W(t)/2 \tag{B.8}$$

where the quantities ℓ_i are the appropriate distances between the positions on the flap.

$$\ell_1 = x_R - x_K \quad , \quad \ell_2 = x_W - x_R \quad , \quad \ell_s = x_K - x_s$$

The following equations define the Δ quantities in (B.8):

$$\Delta x_R \approx \ell_s \left[\frac{\delta C_{p_R}}{C_{p_R}} \left(\frac{u_o u \ell_1}{\sqrt{\pi \bar{u} h \ell_s} e^{-\eta_D^2}} - \frac{1}{2} - C_{p_R} M^2 \right) + \frac{\ell_1^2 \Delta \dot{\theta}_R}{2 \bar{u} h} \right] \qquad \text{(B.9)}$$

$$\approx \ell_s \chi \left[\frac{\delta C_{p_R}}{C_{p_R}} + \frac{N \ell_1 \Delta \dot{\theta}_R}{\theta_R} \right]$$

$$\Delta x_s \approx \ell_s \left[\frac{\ell_1^2 \Delta \dot{\theta}_R}{2 \bar{u} h} + \frac{u_D u \delta C_{p_R}}{2 \bar{u} h \chi} \right]$$

$$\Delta \theta_s \approx - \frac{\Delta x_s}{\ell_s} \tan \theta_s$$

$$\Delta \theta_R \approx - \Delta \theta_W$$

$$\Delta \dot{x}_s \approx \Delta M_s a_\infty$$

$$\Delta \dot{x}_R \approx - \Delta M_R a_\infty$$

Substituting Eqs. (B.5), (B.6), (B.7), and (B.9) into Eq. (B.8) yields a cumbersome criteria for neutral stability. From this one can determine the type of stability observed for a particular motion of the flap.

The above quantities may be interpreted with reference to Fig. B-1. $\Delta p_W(t)$ is the instantaneous pressure change on the flap when it is oscillating through the angle $\Delta \theta_W(t)$.

From the small-angle approximation in supersonic flow and the fact that the disturbance has to travel only one boundary-layer thickness before it affects the free stream, one can state that the corresponding flap force is instantaneous and, consequently, will be damping. The quantity, $x_R(t;t + \Delta t)$, is the movement of the reattachment point on the flap. The pressure difference between the plateau and the final pressure has been designated Δp_R. Both the position and the magnitude of the reattachment pressure involve quantities which change immediately as well as parts which are changed because the upstream parameters of the problem have been altered at the separation point. The latter are termed "upstream communication effects." The final change involves the plateau pressure. It is affected by changing the conditions at the separation point and, therefore, will be lumped into the time-lagged quantities.

The above model and mathematics are extremely simplified versions of the actual phenomenon, but is is consistent with the assumptions used in deriving the initial equation for $\bar{u}$, Equation (B-3). Differentiating the resultant of expression (B.8) with respect to $\Delta\dot{\delta}_R$ and setting it equal to zero determines the phase lags, if any, that are required for neutrally stable oscillations. The equations and the mathematical manipulation involved are rather complex, but some quantitative results indicate that the most adverse conditions exist when the time-lag components are out of phase by one-half cycle. Therefore, depending on the relative magnitudes of the above quantities, self-sustained oscillations are possible with upstream communication time lags giving 1/4 to 3/4 cycle phase lags.

As an example of the above method, one can compute the time lag and the frequency of a separated flow pocket in which the angular changes and accelerated flow effects can be ignored. In this case, the amplifying oscillations may occur if the frequency of oscillation and the separated flow pocket natural frequency concur.

The velocity profile assumed is:

$$u/u_e = \varphi = \frac{1}{2}(1 + \mathrm{erf}_\eta) \qquad \mathrm{erf}_\eta = \frac{2}{\sqrt{\pi}} \int_0^\eta e^{-t^2}\, dt$$

where

$$\eta = \frac{y}{x}$$

$$\sigma = \frac{1}{2}(u_e x/\nu_e \sigma)$$

The shear force is given by Newton's relation

$$\tau_D = \mu \left.\frac{du}{dy}\right|_D = u_D \mu \left(\frac{\sigma}{x}\right) \left.\frac{d\varphi}{d\eta}\right|_D \qquad \text{(B.10)}$$

If one assumes an average-value for τ_D, the form of the above equation reduces to $\tau_D = C\mu u_\infty$, where the constant C has the dimensions 1/length. The value assumed for this example was

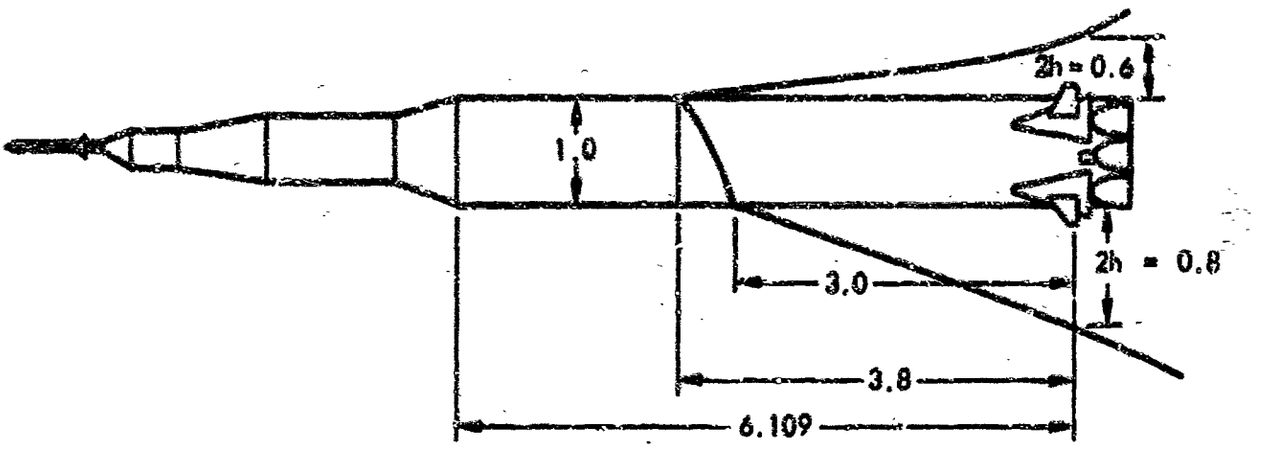
$$\tau_{D_{ave}} = 0.4\, u_e\, \mu_D \,(ft^{-1})$$

and corresponds to a friction coefficient

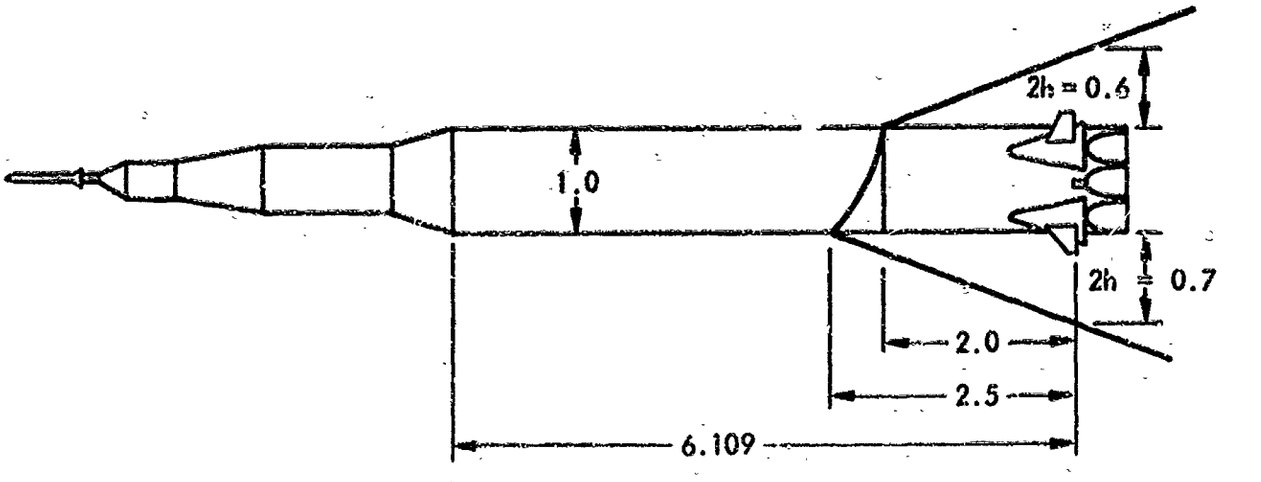
$$C_{f_{ave}} = \frac{0.8\, \nu_D}{u_e} \,(ft^{-1})$$

The exhaust-plume-envelope of the Saturn-Apollo launch vehicles causes extensive separated flow at high altitudes (Refs. 25 and 26 and Fig. B-2). Applying the approximate analysis described above gives

Altitude = 150,000 ft	$f_{crit.}$ = 3.9 and 6.8 cps for top and bottom sides respectively
Altitude = 180,000 ft	$f_{crit.}$ = 9.0 and 5.5 cps for top and bottom sides



a. H = 150,000 FT; M = 5.05; U = 5500 FT/SEC



b. H = 180,000 FT; M = 6.15; U = 6600 FT/SEC

Fig. B-2 Saturn V Plume-Induced Separations

In view of what has been said in the main text about the vertical flow structure, the above values are only approximate. As such, however, they indicate that there could be a coupling between the so called POGO-oscillations (Ref. 28) at about 8 cps and the separated flow pocket. This could also explain the excessive separated flow length at H = 150,000 ft where the pocket frequency is in the critical range. That is, the photograph in Ref. 25 shows the peak extents of flow-separation amplitudes at the top and bottom sides.